INVESTIGATING THE EFFECT OF THICKNESS ON FRACTURE TOUGHNESS OF NITI SHAPE MEMORY ALLOY

A Thesis

by

BASAK ABUT

Submitted to the Office of Graduate and Professional Studies of
Texas A&M University
in partial fulfillment of the requirements for the degree of

MASTER OF SCIENCE

Chair of Committee,	Dimitris C. Lagoudas
Co-Chair of Committee,	Ibrahim Karaman
Committee Member,	Mohammad Naraghi
Head of Department,	Ibrahim Karaman

December 2020

Major Subject: Materials Science and Engineering

ABSTRACT

Shape memory alloys (SMAs) can handle large deformations through martensitic phase transformation and reversible transformation from austenite to martensite under temperature and/or stress changes. Due to their amazing properties, SMAs such as NiTi are increasingly used in a variety of applications where integration requires a complete understanding of fracture mechanics and crack growth behavior. Fracture toughness of conventional metals is believed to be dependent on specimen thickness especially due to the ductile fracture behavior of the material. On the other hand, due to the complex fracture behavior and the phase transformation characteristics of SMAs, the desire to explore the thickness effect on fracture toughness of SMAs arises. In this study, the thickness effect on the fracture toughness of NiTi compact tension (CT) specimens is investigated experimentally. Pre-cracked NiTi specimens with nominal thicknesses changing from 1 mm to 5 mm are used in the fracture experiments under mode-I loading conditions at room temperature at which the material is fully martensite and experiences detwinning upon loading. The resistance curves are obtained from load-displacement data and the J-integral values are determined using a recently proposed methodology for SMAs while the crack sizes are obtained implementing elastic compliance method. Critical J-values for specimens with different thicknesses are obtained from the resistance curves and compared to reveal the thickness dependence of J_{Ic}. The strain fields are measured using the digital image correlation (DIC) technique. This enables investigating the thickness effect by evaluating the zone of nonlinear deformation mechanism near the crack tip.

Based on the critical J-values, thickness is found to have no obvious effect on the fracture toughness of NiTi SMAs within the considered thickness range.

DEDICATION

To my sweet daughter and lovely spouse,

and

to my dear mother.

ACKNOWLEDGEMENTS

I would like to thank my advisor, Dr. Lagoudas, for providing me the opportunity to have this degree and for his valuable guidance throughout the course of this research. I would like to thank my co-advisor, Dr. Karaman, for his great support and pieces of advice for me to continue on my way. I would like to thank Dr. Naraghi, for agreeing to be on my committee.

Thanks also go to my friends and colleagues, Dr. Alexandros Solomou, Dr. Anargyros Karakalas, Dr. Lei Xu, Thianyang Zhou, Dimitrios Loufakis, Paraskevi Flouda, Jobin Joy, and Ralston Fernandes and the department faculty and staff for making my time at Texas A&M University a great experience. My sincere gratitude goes to Dr. Behrouz Haghgouyan for his endless help and support throughout my research. I learned a lot from him and I am grateful for his precious time and bits of advice.

Last but not the least, I would like to thank my family: my sweet little girl, Defne Abut, for making me better, stronger, and fulfilled than I could have ever imagined, my dear husband, Erkan Abut, for his taking up the whole responsibilities to our family, bearing the pressure during my studies, for his never-ending patience and encouragement from beginning to end.

CONTRIBUTORS AND FUNDING SOURCES

Contributors

This work was supervised by a dissertation committee consisting of Professor Dimitris C. Lagoudas of the Department of Aerospace Engineering (advisor), Professor Ibrahim Karaman of the Department of Material Science and Engineering (co-advisor), and Professor Mohammed Naraghi of the Department of Aerospace Engineering.

Funding Sources

This graduate study is supported by AFOSR under Grant Number FA9550-18-1-0276.

Its contents are solely the responsibility of the authors and do not necessarily represent the official views of AFOSR.

NOMENCLATURE

ASTM	American Society for Testing and Materials
COD	Crack Opening Displacement
CT	Compact Tension
DIC	Digital Image Correlation
EDM	Electrical Discharge Machining
EPFM	Elastic Plastic Fracture Mechanics
FEA	Finite Element Analysis
LEFM	Linear Elastic Fracture Mechanics
SMA	Shape Memory Alloy
a	Crack Size
a_0	Initial Crack Size
A_f	Austenite Finish Temperature
A_s	Austenite Start Temperature
A^{el}	Elastic Component of the Area under P-δ Curve
A^{in}	Inelastic Component of the Area under P-δ Curve
b	Unbroken Ligament Length
B	Specimen Thickness
C	Elastic Compliance
da/dN	Fatigue Crack Growth Rate
E	Young's Modulus

E_A	Young's Modulus of Austenite
E_M	Young's Modulus of Martensite
G	Energy Release Rate
J	J-Integral
J_{Ic}	Fracture Toughness
J^{el}	Elastic Component of J-Integral
J^{in}	Inelastic Component of J-Integral
K	Stress Intensity Factor
K_c	Critical Stress Intensity Factor
M_f	Martensite Finish Temperature
M_s	Martensite Start Temperature
M_d	Detwinned Martensite
M_t	Twinned Martensite
P	Applied Load
P_{max}	Maximum Load
P_{min}	Minimum Load
R	Load Ratio
γ^{el}	Elastic Geometry Factor for Crack Growth Correction
γ^{in}	Inelastic Geometry Factor for Crack Growth Correction
δ	Applied Displacement
δ^{el}	Elastic Component of Displacement
δ^{in}	Inelastic Component of Displacement

Δa	Crack Extension
η^{el}	Elastic Geometry-Dependent Factor
η^{in}	Inelastic Geometry-Dependent Factor
σ_y	Yield Stress

TABLE OF CONTENTS

Page

LIST OF FIGURES

Page

LIST OF TABLES

Page

1. INTRODUCTION

Shape memory alloys (SMAs) gain their reputations due to two important features, namely pseudoelasticity and the shape memory effect. These features result from the reversible phase transformation between the high-temperature phase, austenite, and the low-temperature phase, martensite, which can be activated mechanically or thermally [1]. NiTi SMAs are widely used in engineering applications due to these unique properties alongside good mechanical properties. According to a recent review paper [2], understanding the fracture mechanics of SMAs under thermal and mechanical loading is still in its early stages, and more experimental and modeling studies should be performed.

1.1. Phase Transformation in SMAs

The two phases observed in SMAs are the austenite and martensite phases, each with their unique properties and crystal structures [1]. Austenite has generally a cubic structure, while martensite can be monoclinic, orthorhombic, or tetragonal. The transformation from one structure to another structure is occurred by shear lattice distortion and it is known as martensitic transformation. Variants are the different orientations of martensitic crystals during the transformation. Martensitic variants can take two forms: twinned martensite (M^t) and detwinned or reoriented martensite (M^d). Thermally-induced martensite forms in twinned structure, and the twinned structure turns into detwinned structure by deforming the material [1].

The phase transformation in SMAs is reversible: from austenite (parent phase) to martensite (product phase) or vice versa. This reversible transformation constitutes the basic characteristics of SMAs. The phase transformation from austenite to martensite, which is *forward transformation*, is achieved by cooling. Upon heating, martensite transforms back into austenite resulting in the *reverse transformation*.

The characteristic temperatures at which the transformation starts and finishes are listed as martensitic start temperature (M_s), martensitic finish temperature (M_f), austenitic start temperature (A_s), and austenitic finish temperature (A_f). Upon cooling under zero load, austenite begins to transform into twinned martensite at M_s and the transformation is completed at M_f. Similarly, upon heating the transformation from martensite to austenite initiates at A_s and completes at A_f (see Figure 1.1).

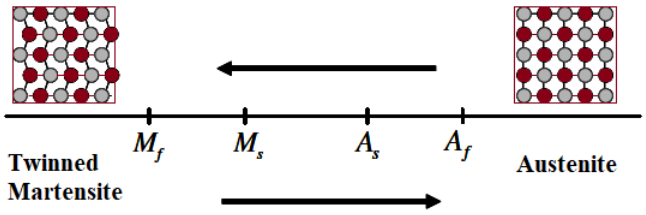

Figure 1.1. Temperature induced phase transformation from austenite to twinned martensite and vice versa without mechanical loading.

In the presence of a mechanical load, the twinned martensite can be detwinned (see Figure 1.2.a). In that case, there will be a visible shape change and the twinned martensite cannot be retained even after the load is released. At this point, heating the SMA above A_f will result in the transformation from detwinned martensite to austenite with a full

shape recovery (see Figure 1.2.b). Cooling back below M_f, austenite will transform to martensite without macroscopic shape change. The process mentioned here is known as the *shape memory effect* of SMAs.

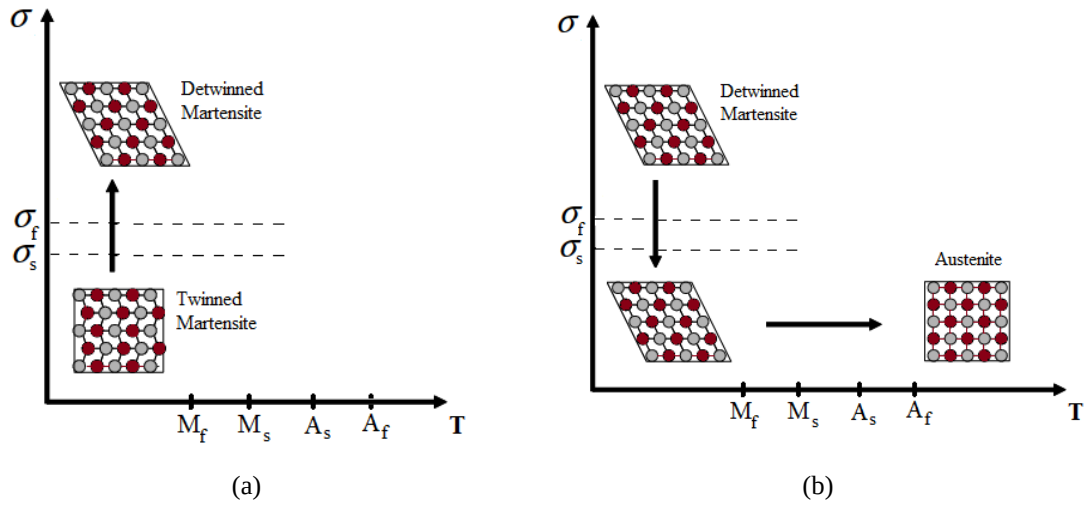

Figure 1.2. Representation of the shape memory effect of an SMA; a) detwinning of martensite under loading, b) unloading and heating to austenite under zero load.

In addition to the above mentioned thermally induced phase transformation, applying a high enough mechanical load can initiate a transformation from austenite to detwinned martensite. When the temperature is kept above A_f during the transformation, it will be possible to achieve a full shape recovery upon unloading to austenite, and this process is known to be the *pseudoelastic effect* (see Figure 1.3.(a)). The corresponding stress-strain plot is given in Figure 1.3.(b).

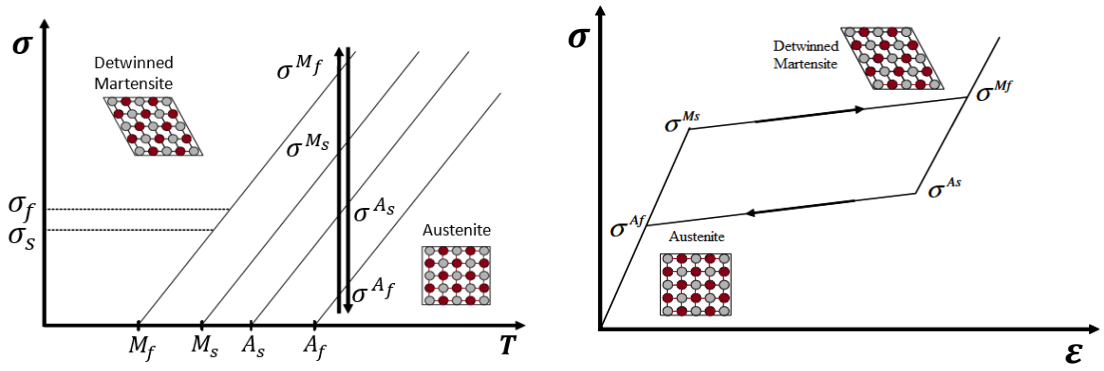

(a) (b)

Figure 1.3. Representation of a) pseudoelastic loading of an SMA, b) pseudoelastic stress-strain plot.

1.2. Literature Review

Although the constitutive behavior of SMAs and the science behind the phase transformation has been investigated considerably, the fracture behavior of SMAs still needs further understanding due to the lack of knowledge on their failure mechanisms. The conventional fracture mechanics theories cannot be applied to SMAs due to their complexity coming from the phase transformation and/or detwinning characteristics. However, most of the studies performed on SMAs base their assumptions on conventional fracture mechanics theories, admitting that these assumptions can be violated by the novel SMA response. The application of the existing studies, although limited in numbers, provides a significant source for understanding the fracture behavior of SMAs.

There are a few experimental studies on the fracture of SMAs, and fracture toughness of NiTi has been investigated in some of them [3-23]. In literature fracture toughness was first cited by Holtz et al. [6] together with their fatigue crack growth results. 12.7 mm thick NiTi plate specimens were used in standard fracture tests at a variety of temperatures. The fracture toughness value was the lowest at ~40 MPa$\sqrt{\text{m}}$ below M_f, where the material was in martensite phase such that there was no superelasticity or phase transformation. As the temperature was increased and the specimens were changed into a mixed-phase condition, the fracture toughness was also increased to 53 MPa$\sqrt{\text{m}}$. When the material reached the superelastic austenite form (above A_f) the fracture toughness was measured to be 65 MPa$\sqrt{\text{m}}$. Gollertan et al. [9] investigated the crack extension under static loading in NiTi SMA CT specimens. They conducted experiments at different temperatures, and the maximum stress intensity factor, K_{max}, obtained at room temperature (martensitic phase) was reported as 31 MPa$\sqrt{\text{m}}$, and the K_{max} value for the pseudoelastic material was found to be 34 MPa$\sqrt{\text{m}}$. In the same experiments, K_{max} value for stable austenitic NiTi SMA was also investigated and found to be increased dramatically to 53 MPa$\sqrt{\text{m}}$ (refer to Figure 1.4).

Edge-cracked sheet specimens were used in the experiments performed by Daly et al. [8]. In their study, the tensile testing was performed on the austenitic NiTi sheets at room temperature and the critical stress intensity value was found to be 51.4 ± 3.6 MPa$\sqrt{\text{m}}$ (refer to Figure 1.5). In the study of Maletta et al. [10, 15], they investigated the crack tip martensitic transformation in a single edge cracked (SEC) NiTi specimen and

looked into the temperature dependence of stress intensity factor at different temperatures within the stress-induced transformation regime. Similar to Gollertan's results, they reported an average critical stress intensity factor of $33.8\ \mathrm{MPa}\sqrt{\mathrm{m}}$ for their NiTi-based pseudoelastic alloy. The material they use was fully austenite at room temperature and all the experiments were conducted above A_f. A slight increase of fracture toughness with increasing temperature was observed which was explained by the toughening effect.

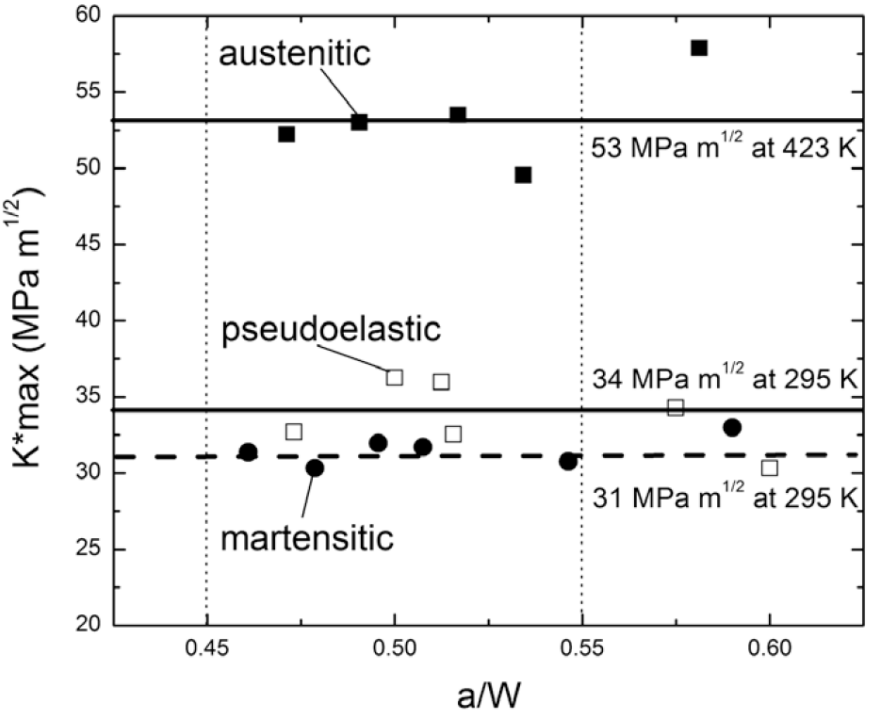

Figure 1.4. Comparison of K_{max} for martensitic, pseduelastic and austenitic NiTi SMAs; after Gollertan et al. [9][*].

[*] Reprinted with permission from "Fracture mechanics and microstructure in NiTi shape memory alloys" by Gollerthan, S., Young, M.L., Baruj, A., Frenzel, J., Schmahl. W. W, and Eggeler, G., 2009. Acta Materialia, 57(4), 1015-1025, Copyright [2008] by Elsevier.

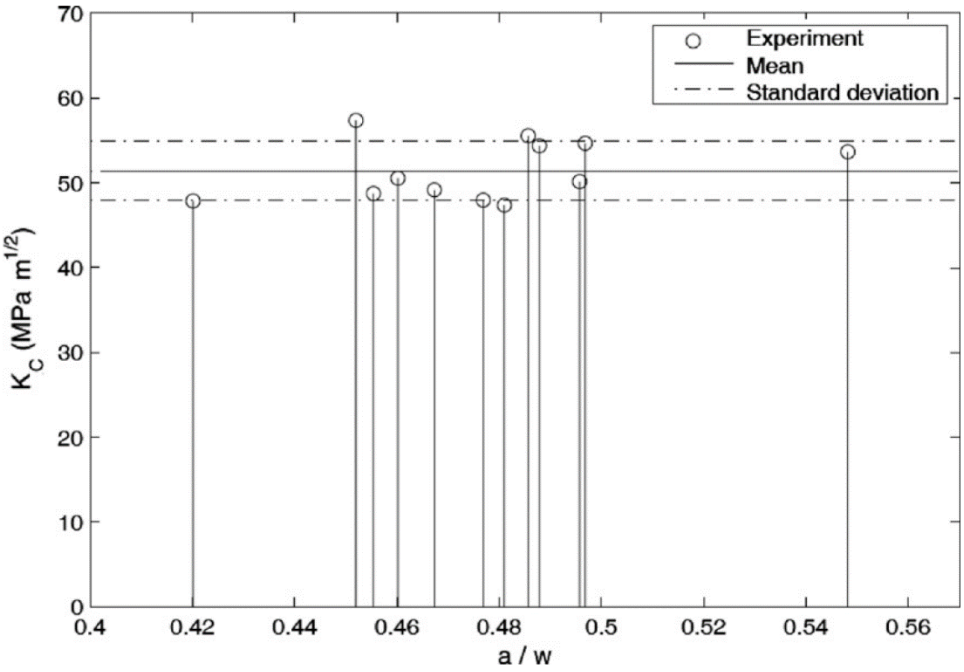

Figure 1.5. K_C values obtained for thin (approx. 150μm) NiTi sheet using a single edge cracked specimen for various values of a/W; after Daly et al. [8][†].

Ahadi et al. [11] studied the grain size dependence of fracture toughness and crack growth resistance of superelastic NiTi with grain size in the range of 10 to 1500 nm. It was reported in their study that there was a monotonic decrease in the fracture toughness and in the crack growth resistance with grain size reduction down to the nanoscale. The phase transformation stress was reported to be increasing gradually with grain size reduction. The strain to failure was also reported to be decreasing with grain size reduction, indicating a reduction in the ductility. The critical stress intensity factor values for the grain size of 1500 nm and 80 nm were found to be $K_{IC} = 46.3$ MPa$\sqrt{\text{m}}$ and 42.4

[†] Reprinted with permission from "An experimental investigation of crack initiation in thin sheets of nitinol" by Daly, S., Miller, A., Ravichandran, G., and Bhattacharya, K., 2007. Acta Materialia, 55(18), 6322-6330, Copyright [2007] by Elsevier.

MPa$\sqrt{\text{m}}$, respectively (refer to Figure 1.6. (a)). When the grain size was reduced to 10 nm, the K_{IC} value was reported as 25.4 MPa$\sqrt{\text{m}}$. Figure 1.6.(b) shows the grain size dependence of crack growth resistance with crack extension. For coarser grains, K_R was reported to have an increasing trend where the crack grew and eventually saturated (rising R-curve). However, for finer grains, the resistance curves were found to be flat. This is because more energy is dissipated during crack propagation for coarser grains while the fracture behavior becomes similar to those of brittle materials for finer grains.

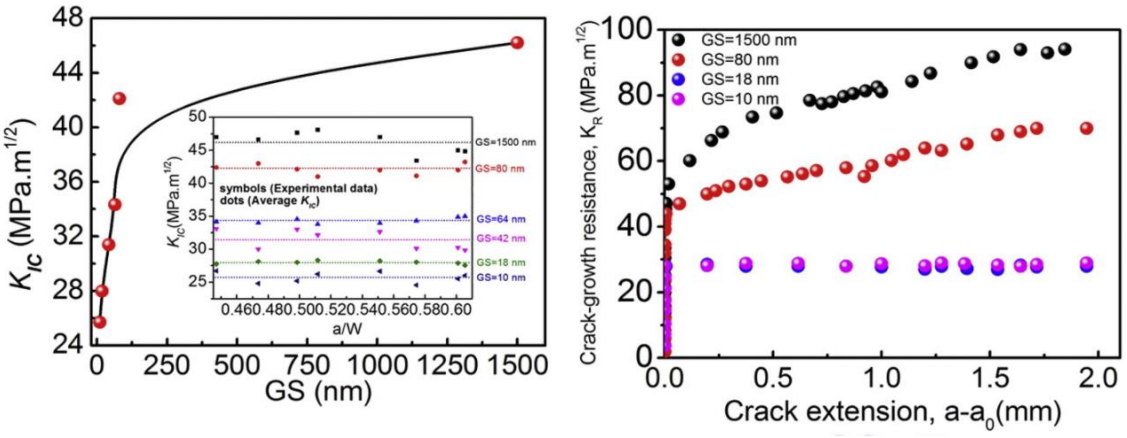

(a) (b)

Figure 1.6. a) Grain size effect on the K_{Ic} for specimens of different initial crack lengths, b) grain size effect on the crack-growth resistance, K_R; after Ahadi et al. [11]‡.

Vaidyanathan et al. [17], Gollerthan et al. [9, 21], and Robertson et al. [7] measured nearly identical fracture toughness values of ~30 MPa$\sqrt{\text{m}}$ for superelastic austenite,

‡ Reprinted with permission from "Grain size dependence of fracture toughness and crack-growth resistance of superelastic NiTi" by Ahadi, A., and Sun, Q., 2016. Scripta Materialia, 113, 171-175, Copyright [2015] by Elsevier.

although they used very different product forms such as bar, plate, and tube, respectively, ranging in thickness values between 0.4 mm to 10 mm.

Apart from the standard fracture toughness testing method, there have been studies using the Digital Image Correlation (DIC) technique to obtain the full-field displacement and measure the fracture toughness [15, 22]. However, the need for more precise imaging equipment, relatively complex test setup, and highly time-consuming post-processing of the measured data makes this method not preferable.

Regarding the fracture toughness of NiTi, the majority of the published studies in the literature are based on the Linear Elastic Fracture Mechanics (LEFM) approach using the ASTM E399 standard [24], assuming small-scale yielding. When performing K_{Ic} tests on standard specimens the following size requirement should be adopted to ensure that plane strain condition prevails: $B \geq 2.5\left(K_{IC}/\sigma_y\right)^2$, where B is the specimen thickness, K_{IC} is the critical stress intensity factor, and σ_y is the yield stress [25]. However, the specimen thicknesses used in the published studies did not exceed the given limit, i.e. the samples used in these studies were not thick enough to comply with the small yielding condition. In the case of SMAs, σ_y should be interpreted as the stress required for the stress-induced transformation/detwinning, not the yield stress. This is because the zone of non-linear deformation, regardless of the mechanism, should be small compared to characteristic dimensions of the crack configuration for LEFM to be valid. For such a requirement to be satisfied, the SMA specimens need to be prohibitively large. Further details are discussed in Appendix A.

Haghgouyan et al. [20] presented a new test methodology for measuring the fracture toughness of NiTi using the critical value of J-integral. The method, based on ASTM E1820 [26] standard, takes into account the martensitic transformation/orientation related changes on the elastic properties of the NiTi SMA material. Fracture experiments were performed using NiTi SMA CT specimens with ~3 mm thickness at three different temperatures, i.e. at 25°C, 80°C and 170°C. The temperatures were selected based on the characteristic phase transition temperatures of the NiTi material so that the material is in full martensite, transforming, and fully austenite form, and the corresponding critical J-values were obtained to be $J_{Ic} = \sim 136\ \text{MPa}\sqrt{\text{m}}$, $\sim 128\ \text{MPa}\sqrt{\text{m}}$ and $\sim 159\ \text{MPa}\sqrt{\text{m}}$, respectively. In this study, in additional to the J-values, the extrapolated $K_{J_{Ic}}$ values were also obtained for the considered testing temperatures as follows: $K_{J_{Ic}} = \sim 95\ \text{MPa}\sqrt{\text{m}}$, $\sim 94\ \text{MPa}\sqrt{\text{m}}$ and $\sim 113\ \text{MPa}\sqrt{\text{m}}$ at 25°C, 80°C and 170°C, respectively. Moreover, the critical stress intensity factors, K_Q, (coming from the LEFM approach) were found to be $K_Q = \sim 38\ \text{MPa}\sqrt{\text{m}}$, $\sim 43\ \text{MPa}\sqrt{\text{m}}$ and $\sim 54\ \text{MPa}\sqrt{\text{m}}$ at 25°C, 80°C and 170°C, respectively (refer to Figure 1.7). The huge difference between $K_{J_{Ic}}$ and K_Q $K_{J_{Ic}}$values explains the inappropriate use of LEFM in determining fracture properties of SMAs. In the present work, the same methodology is implemented where J-integral is used as a fracture criterion, therefore, the requirement on the specimen thickness is not as strict as in the case of K_{IC} experiments.

Reviewing the existing literature, researchers have used specimens with different thickness values. The reported thickness values for either edge-cracked or CT specimens

change from 150 μm to 13 mm as summarized in 1. However, there has been no study using several specimens with different thickness values investigating the thickness effect on fracture toughness of SMAs so far.

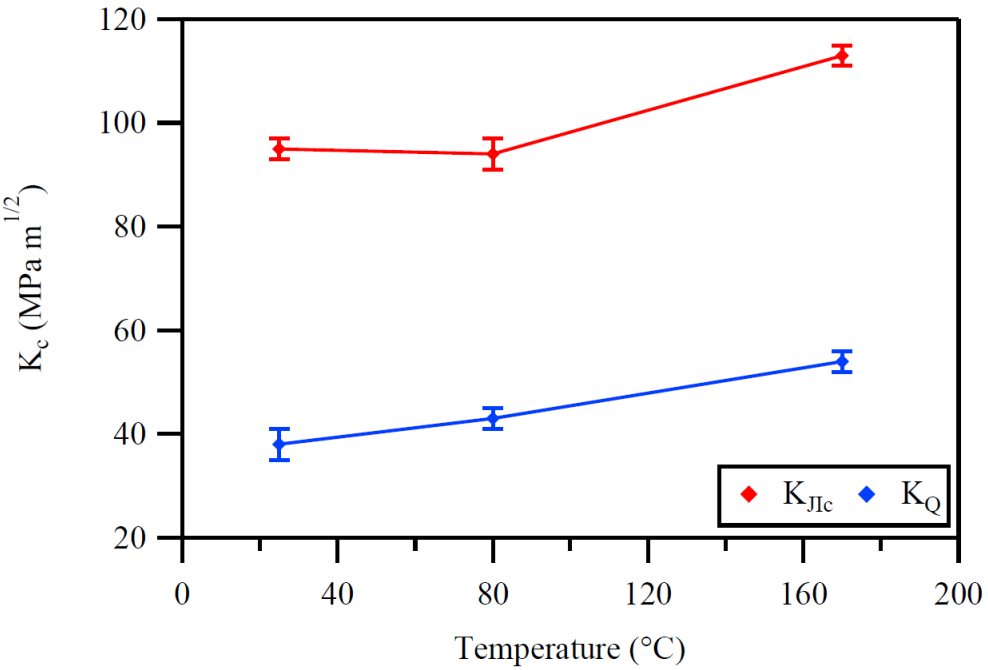

Figure 1.7. K_{JIc} and K_Q values for NiTi CT specimens tested at 25°C, 80°C and 170°C; after Haghgouyan et al. [20][§].

[§] Reprinted with permission from "Fracture toughness of NiTi towards establishing standard test methods for phase transforming materials" by Haghgouyan, B., Hayrettin, C., Baxevanis, T., Karaman, I., and Lagoudas, D.C., 2019. Acta Materialia, 162, 226-238, Copyright [2018] by Elsevier.

Table 1.1. Compilation of all fracture toughness data on NiTi alloys presented in the literature. Adapted from Robertson et al. [14].

		Temperature (°C)					Product				Dimension(mm)		Fracture Toughness
								Type					
Phase	**Reference**	**M_f**	**M_s**	**A_s**	**A_f**	**Test**	**Composition at-%Ni**	**Plate**	**Bar**	**Tube**	**B**	**X***	**K_c (MPa.m$^{1/2}$)**
Martensite	[6]	70	80	100	120	30	49.9				13	51	40
	[17]	35	49	66	86	20	49.4	x			10	50	27
	[21]	10	55	50	85	22	50.3		x		8	16	32
	[9]	16	44	60	84	22	50.3	x			8	16	31
	[6]	70	80	100	120	60	49.9	x			13	51	40
	[20]	42	68	77	106	25	49.5		x		3	20	38
Transforming	[6]	70	80	100	120	120	49.9	x			13	51	53
	[27]	…	…	<20	…	20	49.9				0.5	3	39
	[9]	-63	-44	3	20	22	50.7	x			8	16	34
	[7]	…	…	…	25	37	50.8			x	0.4	12	10-35
	[6]	70	80	100	120	150	49.9	x			13	51	65
	[20]	42	68	77	106	80			x		3	20	43
	[15]	-49	-93	-7	14	20	50.8	x			0.5	50	30
	[15]	-49	-93	-7	14	60	50.8	x			0.5	50	37.5
	[8]	…	…	…	11.3	25	52.0	x			0.15	30	51.4
	[11]	-70	-50	-4.8	10	25	49.1	x			1.7	21	42.4
	[11]	-33	-30	-4.6	3	25	49.1	x			1.7	21	46.3
	[12]	-25	12	-1	2	27	50.8		x		6	15	29
	[16]	-29.1	-23.1	-6.2	6.1	25	50.8	x			0.6	3.9	18-40
Austenite	[9]	-63	-44	3	20	150	50.7	x			8	16	53
	[20]	42	68	77	106	170			x		3	20	54

*X is the global size of the specimen, either diameter or side length.

The thickness range of the specimens is chosen from 2 mm to 5 mm considering some of the previous applications with important contributions in the aviation industry [28-31]. An example of this researches is the work by Mabe et al. [31] that investigates the morphing of variable geometry chevrons using SMAs as actuators. In their study, the thickness of the actuators was in the range of 1.5 mm to 4.4 mm.

The objective of the present study is to further investigate the thickness effect on fracture toughness of near equiatomic NiTi specimens at constant ambient temperature at which the martensitic specimens experience detwinning upon loading. Moreover, the in-plane strains are calculated and compared for NiTi specimens having different thickness values by using the DIC technique.

1.3. Motivation

The fracture toughness is believed to decrease with thickness until it reaches an asymptote where further increase in thickness has no effect on the fracture toughness [25]. Figure 1.8 shows a set of data that belonged to 7075-T6 Aluminum that has commonly been used to demonstrate the thickness effect on fracture toughness. The measured critical fracture toughness value, K_{crit}, decreases with specimen thickness until it reaches a plateau where it becomes insensitive to thickness, and is named as plane strain fracture toughness, K_{Ic} [32]. The decreasing trend of fracture toughness with increasing thickness is a consequence of ductile crack propagation. In such cases, the crack tends to propagate through the regions with high stress triaxiality, slowing down on the outer regions, therefore, forming a flat region in the middle and 45° curved edges as seen in Figure 1.9,

which is a schematic representation of fracture surface morphology for different specimen thicknesses. As the specimen thickness increases, the flat fracture mechanism becomes dominant, and even with a further increase in specimen thickness, the effect on the measured fracture toughness becomes much less. However, the fracture mechanism in SMAs is found to be predominantly cleavage rather than ductile void growth [33, 34]. At this point, it needs further investigation on understanding the thickness effect on fracture toughness of SMAs.

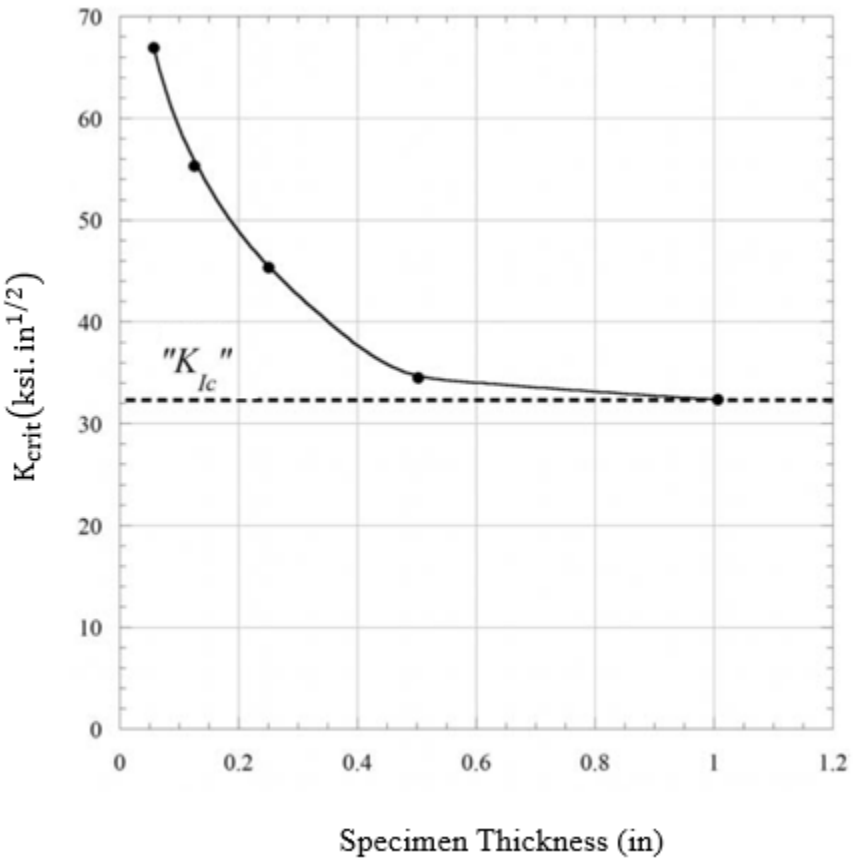

Figure 1.8. Fracture toughness variation with respect to specimen thickness for 7075-T6 Aluminum. Adapted from Barsom and Rolfe [35]

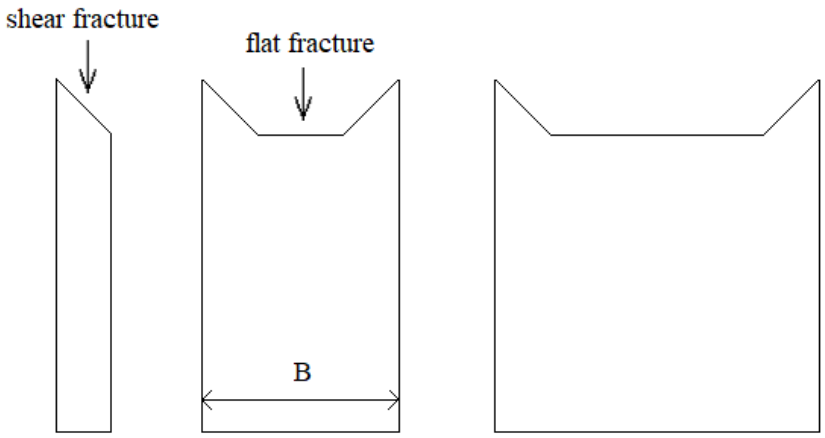

Figure 1.9. Change of fracture surface morphology for ductile crack growth with increasing specimen thickness, B.

Moreover, there are certain thickness criteria given in standards for various specimens and testing methods to determine the plane strain fracture toughness. For example, to determine the fracture toughness calculated from J-R curves the thickness criteria given in the ASTM E1820 standard [26] is: $B > 10J_{Ic}/\sigma_Y$ for a CT specimen, where σ_Y is the effective yield strength (the average of the ultimate tensile strength, σ^{TS}, and the critical stress, σ_{cr}). However, this criterion is defined for conventional materials and needs to be investigated whether it is valid for SMAs.

So far, specimens of different thicknesses have been studied by various numbers of researchers on the determination of fracture toughness of SMAs, and none of the studies have experimented on multiple specimens with changing thicknesses to investigate the thickness dependency of fracture toughness for SMAs. Therefore, the present study will be a pioneer work on understanding the thickness effect on fracture toughness of SMAs.

1.4. Outline

The remainder of the thesis is structured as follows. In Section 2, the methodology for measuring the fracture toughness of SMAs is introduced. Critical J-values were calculated as the fracture toughness parameter. The procedure for how to obtain the resistance curves is described. In Section 3, the material characterization is presented and experimental procedures are explained. This includes the test specimens and the experimental setup. In Section 4, the experimental results from uniaxial tensile experiment and mode-I fracture experiments on specimens with different thicknesses are presented. Resistance curves are plotted, fracture toughness values are obtained. Moreover, the strain maps obtained from DIC are provided. In Section 5, key findings of the study are highlighted and concluding remarks are presented given. Finally, in Section 6, the possible future works are discussed.

2. METHODOLOGY

In this section, the test methodology for measuring the fracture toughness of SMAs is described. This methodology, recently proposed by Haghgouyan et al. [20], uses J-integral as the fracture criterion. It is based on the standard test method ASTM E1820 and takes into account the variations in the elastic properties.

2.1. J-integral Definition

J-integral is a path independent line integral introduced by Rice [36] at the crack tip zone of an elastic-plastic or a nonlinear elastic material. Especially in nonlinear materials, due to the presence of notches and cracks, the determination of concentrated strain fields is mathematically difficult. The choice of a near tip path relates the integral directly to the local concentrated strain field [36].

Considering a homogenous linear or nonlinear elastic material with a notch as shown in Figure 2.1, by neglecting the body forces the strain energy density, W, can be defined by

$$W = W(x, y) = \int_0^{\varepsilon_{ij}} \sigma_{ij} d\varepsilon_{ij} \quad (1)$$

where σ_{ij} and ε_{ij} $\sigma_{ij}$are the stress and strain fields, respectively. Then, the two-dimensional J-integral can be defined as

$$J = \int_{\Gamma} \left(W dy - T_i \cdot \frac{\partial u_i}{\partial x} ds \right) \quad (2)$$

where Γ is an arbitrary contour surrounding the notch tip as shown in Figure 2.1, T_i is the traction vector which is normal along Γ, $T_i = \sigma_{ij} n_j$, u_i is the displacement vector, and ds is the infinitesimal arc length along Γ.

When Γ is taken close to the notch tip, the traction vector will be vanished ($\mathbf{T} = 0$) and the integral will depend only on the local field, reducing to:

$$J = \int_{\Gamma_t} W dy \quad (3)$$

where Γ_t is the path taken at the tip of a crack and J becomes the averaged strain value at the notch tip [36].

It should be noted that the J-integral is path independent and for the special case of a linear elastic material, it is equivalent to the energy release rate, G, which was proposed by Irwin [37]. Moreover, the J contour integral has succeeded to be a fracture characterizing parameter, becoming both an energy parameter and a stress intensity parameter, extending the limits of LEFM [25].

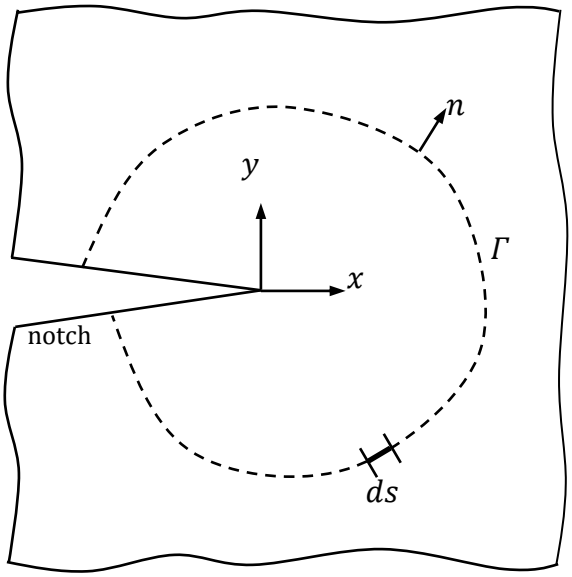

Figure 2.1. Representation of a notched specimen in 2D deformation field and Γ being the path surrounding the notch tip

Considerable experimental studies were conducted to develop functional test methods for determining the critical J value, J_{Ic}, for opening cracks under mode-I loading [38]. Pioneer studies were conducted by Begley and Landes [39, 40] using the energy principle on CT specimens, and the critical J value under mode-I loading conditions were successfully measured. In their study, a series of CT specimens with the same geometry but different crack sizes were tested, the absorbed energy was determined and the corresponding J-values were calculated [39]. The main drawback of this method is the requirement of multiple specimens to obtain a single value of J. Even so, these early studies encouraged the researchers and J-integral was recognized as a measurable parameter for determining the fracture toughness of ductile materials [38].

The most remarkable work in evaluation of J-integral came from Rice [41] by using the load-displacement curve obtained from a single specimen. It was proposed that the strain energy can be obtained from the area under the load-displacement curve, thus, the J-integral can be defined as:

$$J = -\frac{1}{B}\int_0^{\Delta}\left(\frac{\partial P}{\partial a}\right)_{\Delta} d\Delta \tag{4}$$

under displacement control, and

$$J = \frac{1}{B}\int_0^{P}\left(\frac{\partial \Delta}{\partial a}\right)_{P} dP \tag{5}$$

under load control condition where B is the specimen thickness, a is the crack length, P is the load, and Δ is the corresponding load point displacement. There will be a bending moment due to the applied load, P, and it will be supported by the remaining ligament, b, $(b = W - a)$, then the J-integral can be estimated as:

$$J = \frac{2}{Bb}\int_0^{\Delta} P d\Delta = \frac{2A_{tot}}{Bb} \tag{6}$$

where A_{tot} is the total area under load-displacement curve, representing the energy absorbed by the specimen [38]. Landes et al. [42], considering the calculated A_{tot} value, proposed that Eq.6 was still applicable with reasonable accuracy for CT specimens with

deep cracks and ASTM E399 three-point bending specimens, even when the load point displacement was replaced with the load line displacement (LLD). Thus, the relation given in Eq.6 becomes an important step towards making the J-integral test a practical testing method .

2.2. Calculation of J-integral

The expression used to measure the J-values during the loading history is first given for the stationary cracks, then modified for the advancing cracks.

2.2.1. Stationary cracks

For stationary cracks, the J-values, composed of elastic and inelastic components, can be calculated from the load-displacement data of a CT specimen.

$$J = J^{el} + J^{in} = \frac{\eta^{el} A^{el}}{Bb} + \frac{\eta^{in} A^{in}}{Bb} \tag{7}$$

where η^{el} and η^{in} are dimensionless constants and will be discussed further in Appendix B, A^{el} and A^{in} are the elastic and inelastic parts of the area under the load-displacement curve, respectively.

In conventional elastic-plastic materials, the elastic J can be computed using the relation of Griffith's strain energy release rate [43], $G = K^2(1-\nu^2)/E'$ where K is the stress intensity factor, ν is the Poisson's ratio, and $E' = E$ and $E' = E/(1-\nu^2)$ for plane stress and plane strain conditions, respectively. However, in SMAs the Young's modulus takes different values as the material transforms into different phases. Therefore, the

determination of η^{el} component becomes a necessity for calculating the elastic part of the J-integral.

2.2.2. Advancing cracks

For advancing cracks, the J-values, composed of elastic and inelastic parts, can be measured at each loading increment by implementing the compliance values evaluated from each loading path of the load-displacement data using the following expression [44]:

$$J = J_i^{el} + J_i^{in} \tag{8}$$

There is a continuous change in the crack length throughout the test, therefore, the J-integral is needed to be calculated incrementally, i.e. at each unloading point. The corresponding elastic and inelastic components of the J-values are as the following;

$$J_i^{el} = \left[J_{i-1}^{el} + \frac{\eta_{i-1}^{el}}{Bb_{i-1}} A_{i-1,i}^{el}\right]\left[1 - \frac{\gamma_{i-1}^{el}}{b_{i-1}}(a_i - a_{i-1})\right] \tag{9}$$

$$J_i^{in} = \left[J_{i-1}^{in} + \frac{\eta_{i-1}^{in}}{Bb_{i-1}} A_{i-1,i}^{in}\right]\left[1 - \frac{\gamma_{i-1}^{in}}{b_{i-1}}(a_i - a_{i-1})\right] \tag{10}$$

At each i^{th} step, J^{el} and J^{in} are calculated from the previous step. γ^{el} and γ^{in} are geometry dependent constants and can be calculated by using η^{el} and η^{in}, respectively. The calculation of the geometry dependent factors, γ^{el} and γ^{in} are given in Appendix B.

$A_{i-1,i}^{el}$ and $A_{i-1,i}^{in}$ are the incremental areas of the elastic and inelastic parts under the load-displacement curves, respectively (see Figure 2.2), calculated from the previous step, $i-1$ to the current step, i. The incremental areas can be calculated as the following:

$$A_{i-1,i}^{el} = \frac{1}{2}(P_i + P_{i-1})\left(\delta_i^{el} - \delta_{i-1}^{el}\right) \tag{11}$$

$$A_{i-1,i}^{in} = \frac{1}{2}(P_i + P_{i-1})\left(\delta_i^{in} - \delta_{i-1}^{in}\right) \tag{12}$$

where P_{i-1} and P_i are the load values at the previous and the current step, respectively. Displacement is composed of elastic and inelastic components such as $\delta_i^{el} = P_i C_i$ and $\delta_i^{in} = \delta_i - \delta_i^{el}$ where C_i is the elastic compliance calculated at each unloading step.

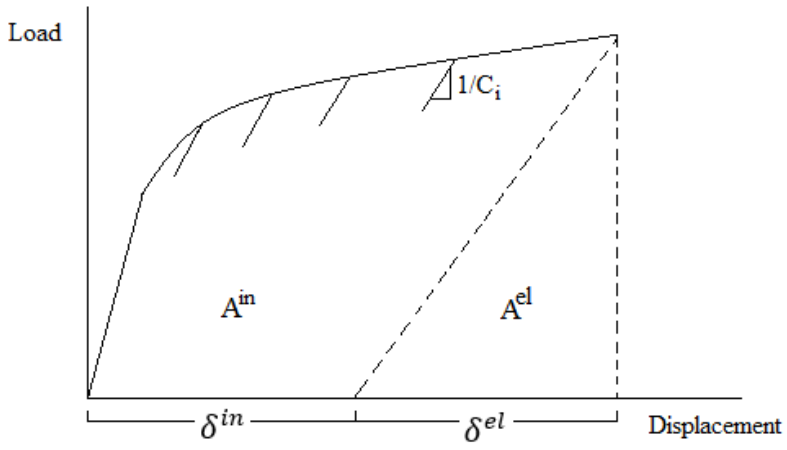

Figure 2.2. Definition of A^{in}, A^{el}, δ^{in} and δ^{el} and compliance, C_i, at each loading step

2.3. Calculation of Crack Size

Optical measurement, compliance method, and electrical potential method are the most commonly used techniques in experimental studies to determine the crack size [45]. Regarding optical measurement, monitoring the crack length at certain intervals requires accurate measurements, and it is straightforward. However, it requires advanced monitoring technologies. The electrical potential or the potential drop method is another accurate and efficient technique for determining the crack size. This method is based on the distortion of the electrical potential field due to any discontinuity in the current-carrying body, and the magnitude of the distortion depends on the size and the shape of the discontinuity. As the crack grows, the remaining uncracked ligament of the specimen decreases, thus, its electrical resistance increases, resulting in an increase in the potential difference between two points surrounding the crack. Comparing the increasing potential with a reference potential value will lead to the crack length with the use of corresponding calibration curves for particular specimen geometries. However, the accuracy of this method may be limited due to the electrical stability, the resolution of the measurement system and the rough contact between the crack surfaces. The high machining requirement, difficult calibration processes and the change in electrical resistivity with increasing plastic deformation and phase transformation in SMAs are the other challenging factors [45]. In the compliance method, the displacement between two load points, is directly proportional to the applied load at the corresponding points, for a given crack size under linear elastic conditions and defined as compliance. Furthermore, the crack size can be determined using the relation, $BEC = f(\frac{a}{W})$, between the dimensionless

compliance and the dimensionless crack size, where $f\left(\frac{a}{W}\right)$ is a geometry dependent shape function.

In the current study, the elastic compliance method was implemented. It was first introduced by Clarke [46] and was further improved by Joyce and Gudas [47]. The crack size for each step of the loading/unloading sequence can be computed using the following relation from the study of Saxena and Hudak [48]:

$$\frac{a_i}{W} = 1.000196 - 4.06319(U) + 11.242(U)^2 - 106.043(U)^3 + 464.335(U)^4 - 650.677(U)^5 \quad (13)$$

The optimum fit was achieved using the function $U = 1/\left(\sqrt{BEC_i} + 1\right)$. Since in SMAs the Young's modulus, E, takes different values as the material transforms into different phases, E should be selected according to the phase at the nominal testing temperature at which the experiments are performed.

2.4. Determining the Fracture Toughness

Resistance curve (R-curve) is a plot of crack growth resistance as a function of crack extension. As stated before, the resistance curve can be obtained from a single specimen using loading-unloading sequences of a load-displacement curve. After obtaining the resistance curve, a construction line is plotted in accordance with the $\frac{J}{\Delta a} = 2\sigma_Y$ relation, where σ_Y is the effective yield strength (the average of the ultimate tensile

strength, σ^{TS}, and the critical stress, σ_{cr}). In general, the critical stress can be the yield stress, σ_y, for an elastic-plastic material, or the detwinning start stress, σ_s, or the phase transformation start stress, σ^{M_s}, for SMAs. The slope of the construction line is intended to represent the component of crack extension that is due to crack tip blunting, rather than ductile tearing. Then, two exclusion lines are drawn parallel to the construction line with x-intersection points at 0.15mm and 1.5mm. The data points falling in the defined region enclosed by the exclusion lines are the qualified data points. These limits are imposed because beyond certain values the fracture parameter may no longer represent the crack tip field. Figure 2.3 typically illustrates a resistance curve.

A regression line, which is the power-law fit $J = C_1 \left(\frac{\Delta a}{k}\right)^{C_2}$ to the qualified data points, where $k = 1.0$ mm, C_1 and C_2 are the power-law coefficients, is drawn, and a line parallel to the construction line with an x-intersection point at 0.2 mm is plotted in accordance with ASTM E1820 [26]. The critical J-value, J_{Ic}, can be obtained at the initiation of stable crack growth which is the intersection point of the regression line and the 0.2 mm offset line. [38].

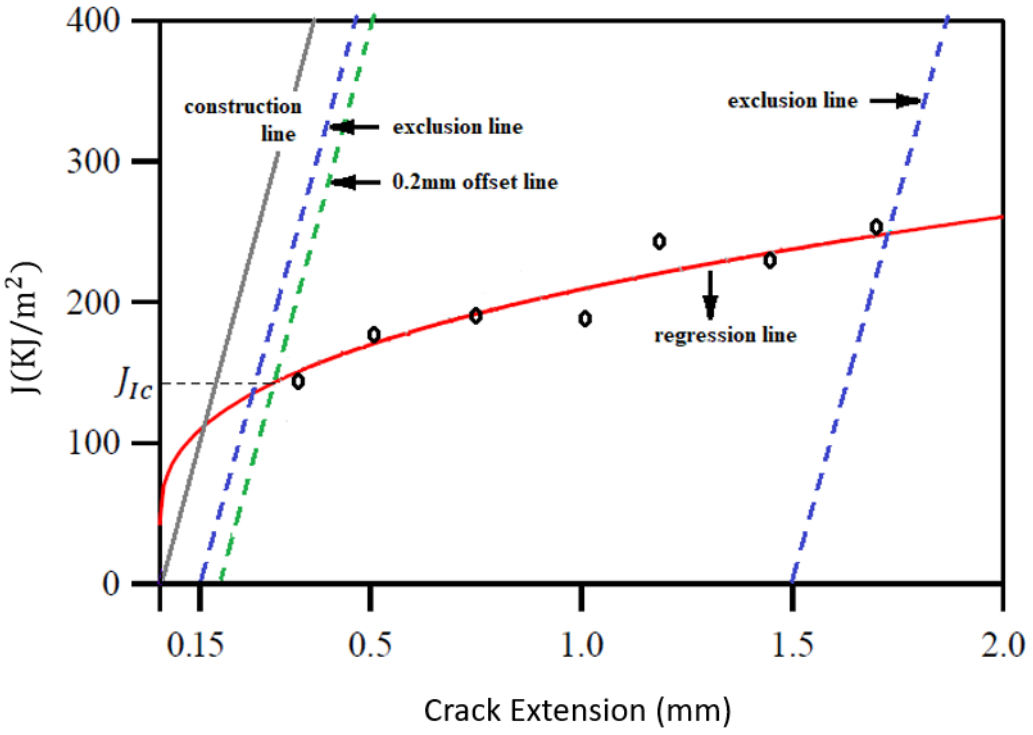

Figure 2.3. Representation of construction line, exclusion lines and power-law fit regression line used in resistance curve method.

3. EXPERIMENTAL

3.1. Material

A near-equiatomic $Ni_{49.5}Ti_{50.5}$ (at.%) obtained from ATI was investigated. The NiTi rod was initially hot forged at 800°C, proceeded by air cooling. A TA Q2000 Differential Scanning Calorimetry (DSC) instrument was used to determine the transformation temperatures; M_s, M_f, A_s, and A_f. A heat/cool cycle was carried out at a rate of $10°C/min$ keeping the temperature range between $0°C$ to $150°C$. The corresponding DSC curve and the obtained transformation temperatures using tangent lines are plotted in Figure 3.1. The characteristic phase transformation temperatures were found to be $M_s = 68°C$, $M_f = 42°C$, $A_s = 77°C$ and $A_f = 106°C$.

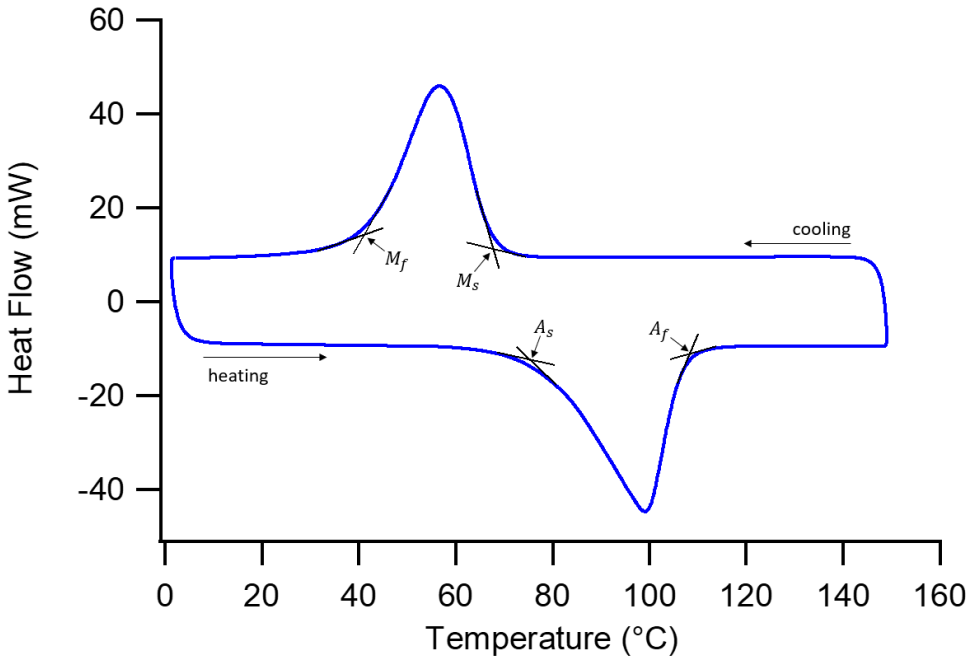

Figure 3.1. DSC curve for the NiTi SMA sample, M_f = 42°C, M_s = 68°C, A_s = 77°C and A_f = 106°C.

3.2. Specimen

Dog-bone samples were cut using Electrical Discharge Machining (EDM). The schematic of the dog-bone sample is shown in Figure 3.2. Tensile characterization was performed on dog-bone samples until failure with a servo-hydraulic MTS test frame at a strain rate of $5x10^{-4}s^{-1}$.

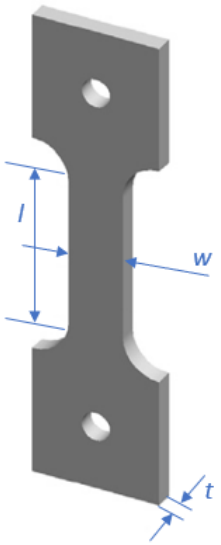

Figure 3.2. Schematic of the dog-bone specimen for tensile characterization experiments with l = 8, w = 3, $\mathbf{0.75} \leq \boldsymbol{t} \leq \mathbf{1.5}$, all in mm.

NiTi compact tension (CT) specimens with five different nominal thickness values (1, 2, 3, 4, 5 mm) were cut using Electrical Discharge Machining (EDM) as shown in Figure 3.3. A total of 15 specimens were tested, i.e. 3 tests for each thickness value. Since 1 mm thick specimens were buckled during the fracture experiments, their results were not taken into account. The load-displacement curves for 1 mm thick specimens showing the apparent buckling behavior are presented in Appendix C.

Figure 3.3. A set of NiTi CT specimens with nominal thickness values from 1mm to 5mm (from right to left)

Prior to the fatigue pre-cracking experiments, the samples were prepared by mechanical grinding with the use of abrasive papers, then polished to the perfect finish. The most important purpose of polishing the samples is to obtain a highly reflective surface without scratches, which will improve the monitoring results recorded throughout the experiments.

The schematic of the CT specimen is given in Figure 3.4, where B is the actual thickness after polishing, a_0 is the initial crack length at the end of the pre-cracking (the total distance measured from the load line including the pre-crack size), and W is the width of the specimen ($W = 20$ mm for all specimens). In accordance with ASTM E1820 [24], all crack sizes were kept between $0.45 < a/W < 0.55$ at the end of the pre-cracking. The test matrix is given in Table 3.1, where the specimens are enumerated considering their thickness values.

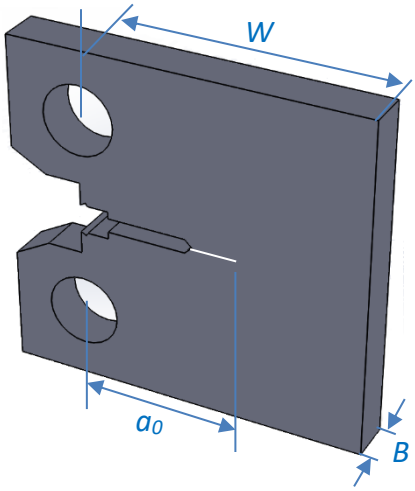

Figure 3.4. Schematic representation of the CT specimen dimensions where *B* is the specimen thickness, *W* is the width measured from the load line (*W* = 20 mm) and a_0 is the initial crack size.

Table 3.1. Test matrix of NiTi CT specimens where *B* is the nominal thickness, a_0 is the initial crack size (the total distance from the load line including the pre-crack size) and *W* is the width of the specimen (*W* = 20 mm). *a/W* ratio is kept between 0.45 < *a/W* < 0.55.

Nominal Thickness	**Specimen #**	***B* [mm]**	**a_0 [mm]**	***a/W***
2 mm	Specimen 1	1.85	9.16	0.46
	Specimen 2	1.84	9.91	0.50
	Specimen 3	1.82	9.72	0.49
3 mm	Specimen 4	2.87	9.12	0.46
	Specimen 5	2.81	9.21	0.46
	Specimen 6	2.81	9.21	0.46
4 mm	Specimen 7	3.83	9.28	0.46
	Specimen 8	3.87	9.77	0.49
	Specimen 9	3.82	9.74	0.49
5 mm	Specimen 10	4.86	9.47	0.47
	Specimen 11	4.92	9.58	0.48
	Specimen 12	4.85	9.47	0.47

3.3. Procedure

Prior to fracture experiments, a sharp fatigue crack that is long enough to diminish the notch effect should be introduced to the crack tip. Fatigue pre-cracking was performed by a servo-hydraulic test frame (MTS model 810), equipped with a 10 kN load cell, with load values between P_{min} and P_{max}, with a load ratio of $R = P_{min}/P_{max} = 0.1$ at 10 Hz frequency. P_{min}/P_{max} values were $80N/800N$, $120N/1200N$, $160N/1600N$ and $200N/2000N$ for 2 mm, 3 mm, 4 mm and 5 mm thick specimens, respectively. The pre-crack size was kept ~1 mm. Number of cycles until the required pre-crack size achieved were between 18000 to 28000 for all specimens.

Mode-I fracture experiments were conducted under displacement-control in the same test frame at a loading rate of 0.4 mm/min. Load and displacement, which was measured directly from the load line using a crack opening displacement (COD) gauge, were recorded throughout the test. Unloading/reloading cycles were carried out to determine the specimen compliance. Referring to the ASTM E1820 standard, the compliance values were corrected due to the sample rotation. The tests were performed at room temperature, which is below M_f, therefore, the NiTi material is fully martensite during the experiments and detwinning occurs upon loading. The test frame with the measuring and recording equipment is illustrated in Figure 3.5.

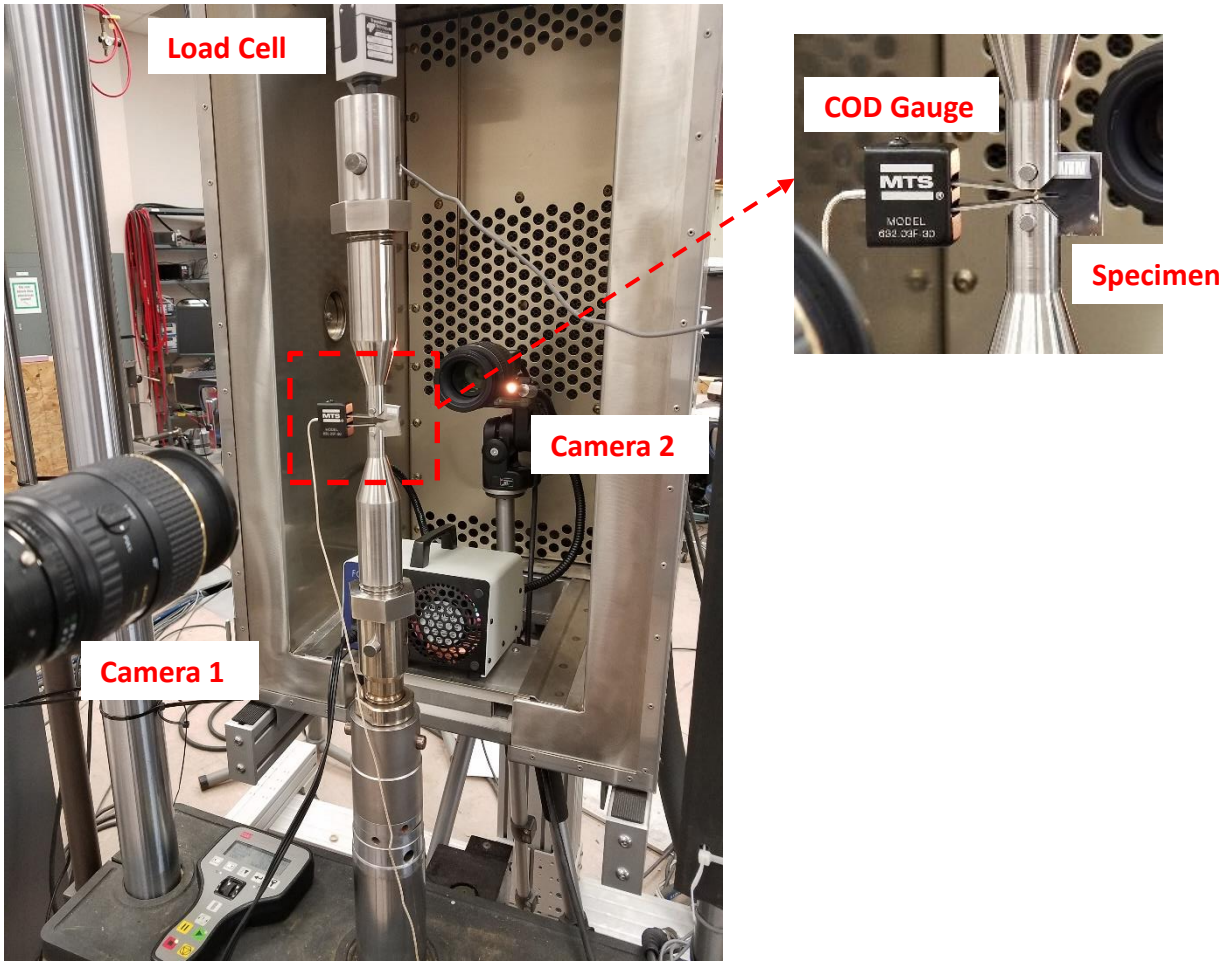

Figure 3.5. Test setup for fracture experiments having two cameras at the front and at the back to record the crack growth and DIC data, respectively. A COD gauge was used to measure the crack tip opening displacement.

The DIC technique was used to measure the full-field strain distribution on the surface of the specimen. DIC is a non-contact, image-based technique used to measure strains and displacements on the surface of the specimen. In the DIC test, the digital images captured at different stages of the test are compared with the reference image taken before the test begins. Further details about DIC can be found in the study of Schreier et

al., [49]. One side of the specimen was sprayed with white paint, and then black speckles were introduced on the white surface randomly by using a black spray. Continuous recording of images was performed on the speckled surface of the specimen at 1 Hz by a Two Point Grey CCD camera equipped with Tokina AT-X PRO lenses, resulting in an optical resolution of 0.02 mm/pixel. Vic2D-6 software was used for the post-processing of the images.

4. RESULTS AND DISCUSSION

4.1. Stress-Strain Response

The stress-strain response of a NiTi SMA dog-bone sample at room temperature is plotted in Figure 4.1. Three experiments were performed, the figure presents the response of a single specimen. In the first stage, the martensite deformed elastically and the Young's modulus obtained from the initial loading path (up to 50MPa) was ~67 GPa, which corresponds to the purely martensitic phase (denoted as E_M). The elastic deformation continued until detwinning took place where it showed itself as a stress plateau at approximately $\sim$203 MPa. After the stress plateau, as the load increased, the reoriented martensite continued to deform and the main deformation mechanism was elastic. Upon further loading, the deformation changed into plastic and reached the ultimate stress at approximately $\sim$950 MPa and then failure occurred. A considerable elongation (~40% elongation) was observed. The tensile properties are summarized in Table 4.1.

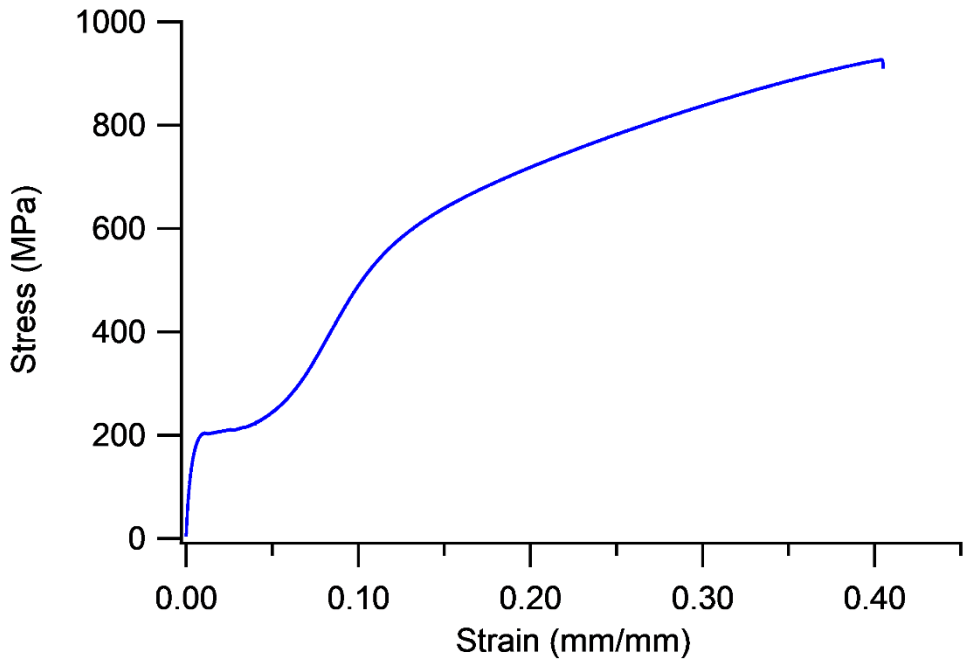

Figure 4.1. Stress-strain response of the NiTi SMA dog-bone sample tested at room temperature.

Table 4.1. Uniaxial tensile characterization results for NiTi dog-bone specimens tested at room temperature.

Properties	
Martensitic Young's Modulus, E_M	$67 \pm 3\ GPa$
Detwinning Start Stress, σ_s	$203 \pm 7\ MPa$
Ultimate Tensile Strength, σ^{TS}	$950 \pm 16\ MPa$
Total Elongation, ε_f	$40 \pm 3\ \%$

4.2. Load-Displacement Data

The experimental load-displacement data for NiTi CT specimens under mode-I loading are plotted in Figure 4.2 (a), (b), (c), and (d) for 2 mm, 3 mm, 4 mm, and 5 mm specimens, respectively. Since the specimens with 1mm nominal thickness were buckled during the experiments, the corresponding data were not taken into consideration. The results for buckled samples are presented in Appendix C. Three experiments have been conducted for each thickness value to show that the results are reproducible and consistent. Stable crack growth was observed during the experiments. The response was linear in the first stage, then reached to a maximum point and then dropped gradually. The growing divergence from linearity was due to the detwinning of martensite. In our case, due to the significant deviation from linearity, the non-linear region in the crack tip was expected to be large enough compared to the characteristic dimensions of the specimen, thus, the Elastic Plastic Fracture Mechanics (EPFM) and the use of J-integral were considered in the calculations.

Since stable crack growth was observed in all experiments, the J-integral should be calculated incrementally. Thus, we need to unload and reload the specimen at certain intervals. The elastic compliance was calculated at each unloading path of the load-displacement data plotted in Figure 4.2. In order to obtain more accurate results, the compliance data was corrected for the rotation of the sample according to ASTM E1820. The details are given in Appendix D.

(a)

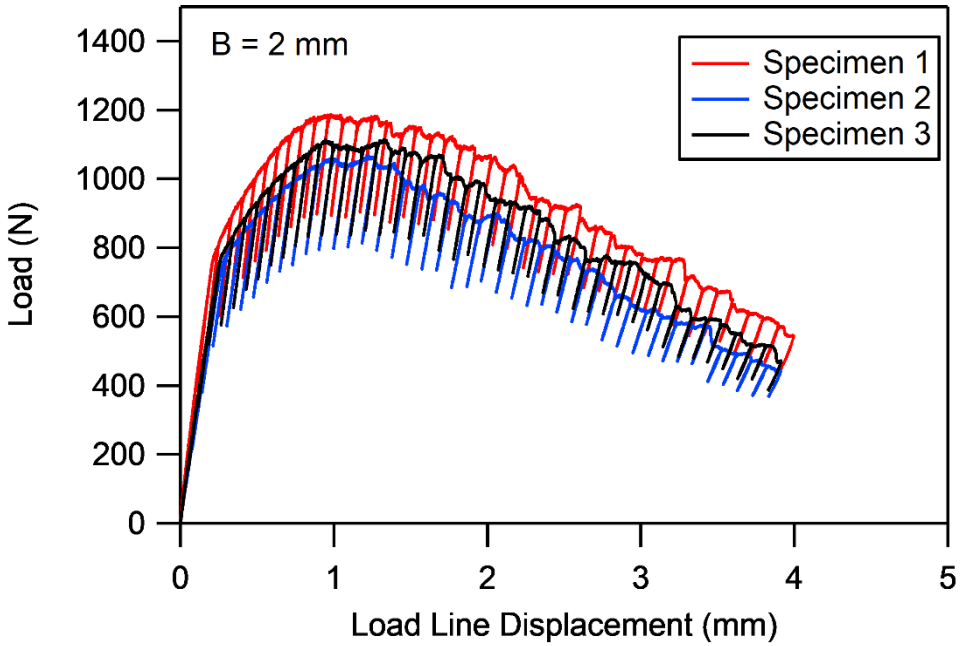
B = 2 mm
Specimen 1
Specimen 2
Specimen 3
Load (N)
Load Line Displacement (mm)
0
200
400
600
800
1000
1200
1400
0
1
2
3
4
5

(b)

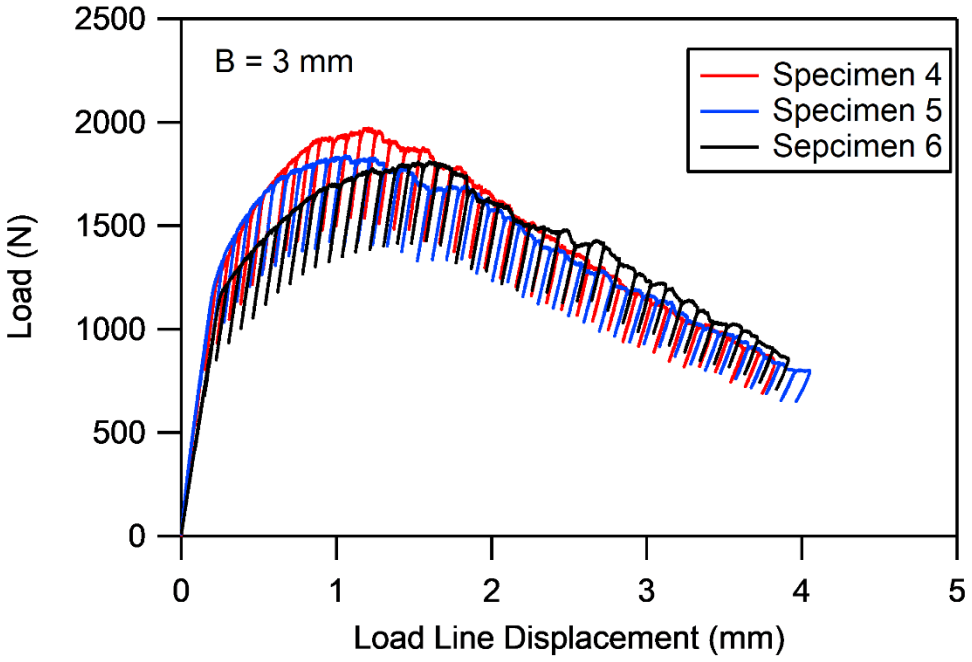
B = 3 mm
Specimen 4
Specimen 5
Sepcimen 6
Load (N)
Load Line Displacement (mm)
0
500
1000
1500
2000
2500
0
1
2
3
4
5

(c)

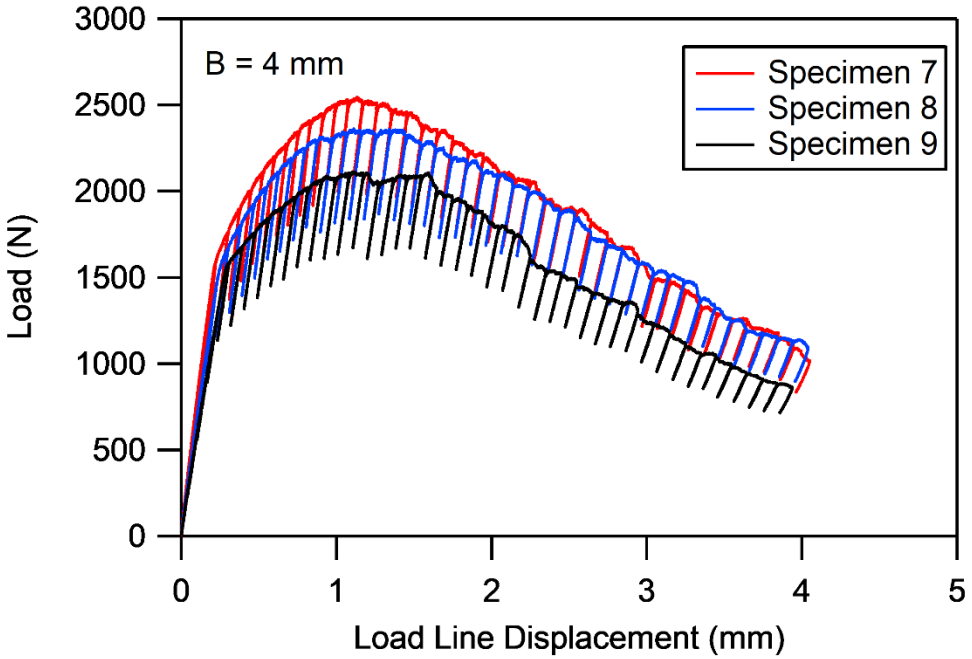

(d)

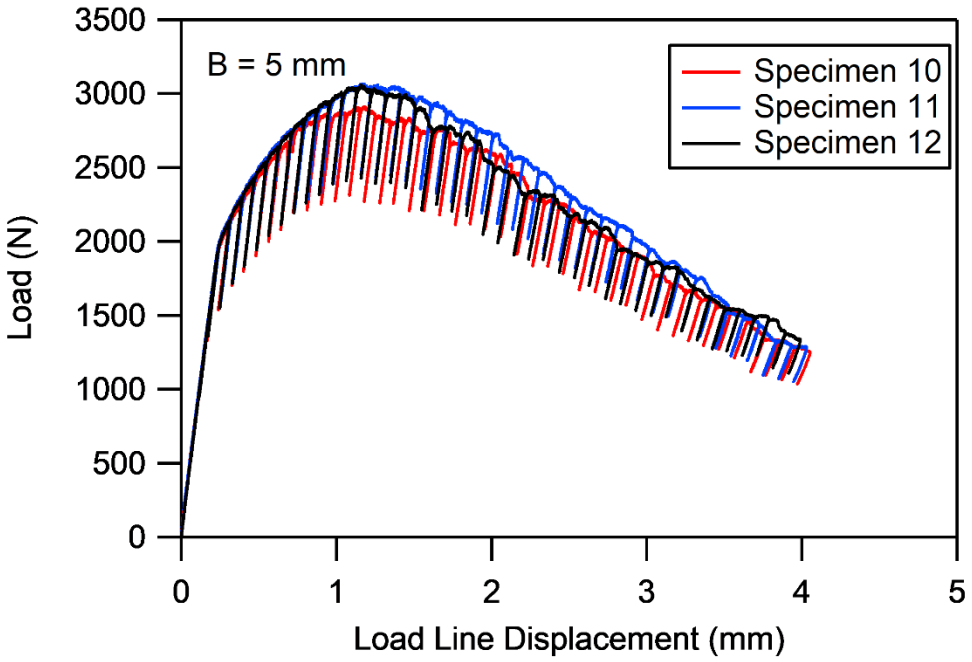

Figure 4.2. Load-displacement curves for NiTi specimens tested at room temperature under mode-I loading with four different thickness values: (a) 2mm, (b) 3mm, (c) 4mm, (d) 5mm

4.3. Resistance Curves

To measure the resistance of the material to crack extension, resistance curves (*J-R* curves) were plotted with the calculated J-values and the corresponding crack extensions (Δa). The results are plotted in

Figure 4.3(a), (b), (c) and (d) for 2 mm, 3 mm, 4 mm and 5 mm, respectively. In accordance with the ASTM E1820 procedure, a construction line is drawn at the origin with a $2\sigma_Y$ slope. Then, two exclusion lines are drawn parallel to the construction line intersecting the x-axis at 0.15 mm and 1.5 mm. The data points in between these exclusion lines are qualified data points and a regression line is drawn using the power-law fit. J_{Ic} values can be determined by taking the intersection point of the 0.2 mm offset line and the aforementioned regression line.

The rising R curve behavior can clearly be seen in Figure 4.3 for all thickness values. Since the inelastic deformation zone at the crack tip is large compared to the relevant dimensions of the specimen and increases in size as the crack grows, the driving force should be increased to maintain the crack growth, resulting in the rising *R*-curve behavior [25].

(a)

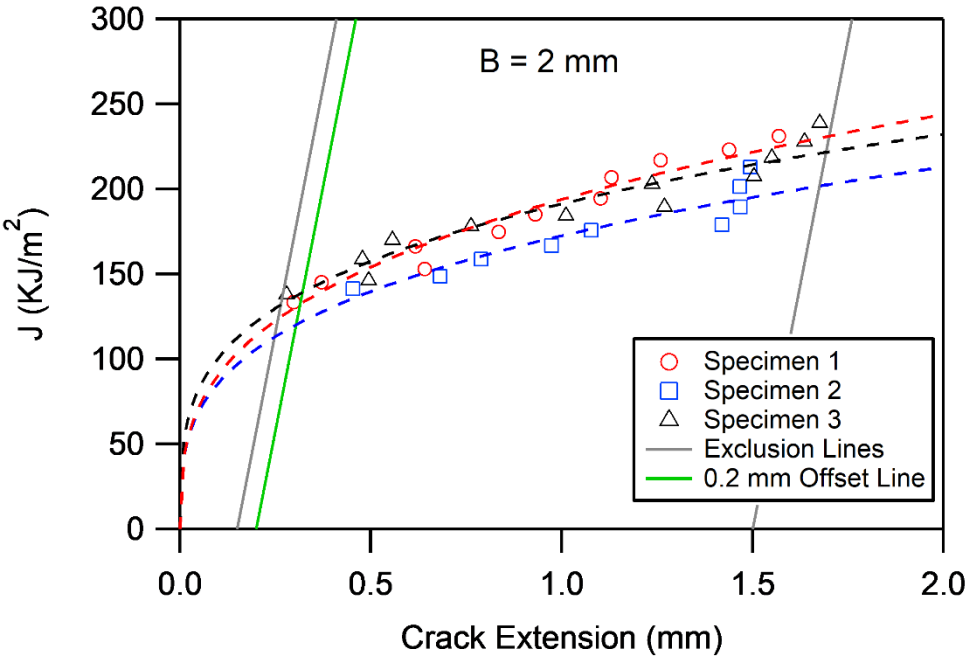
B = 2 mm
J (KJ/m^2)
Crack Extension (mm)
Specimen 1
Specimen 2
Specimen 3
Exclusion Lines
0.2 mm Offset Line
0
50
100
150
200
250
300
0.0
0.5
1.0
1.5
2.0

(b)

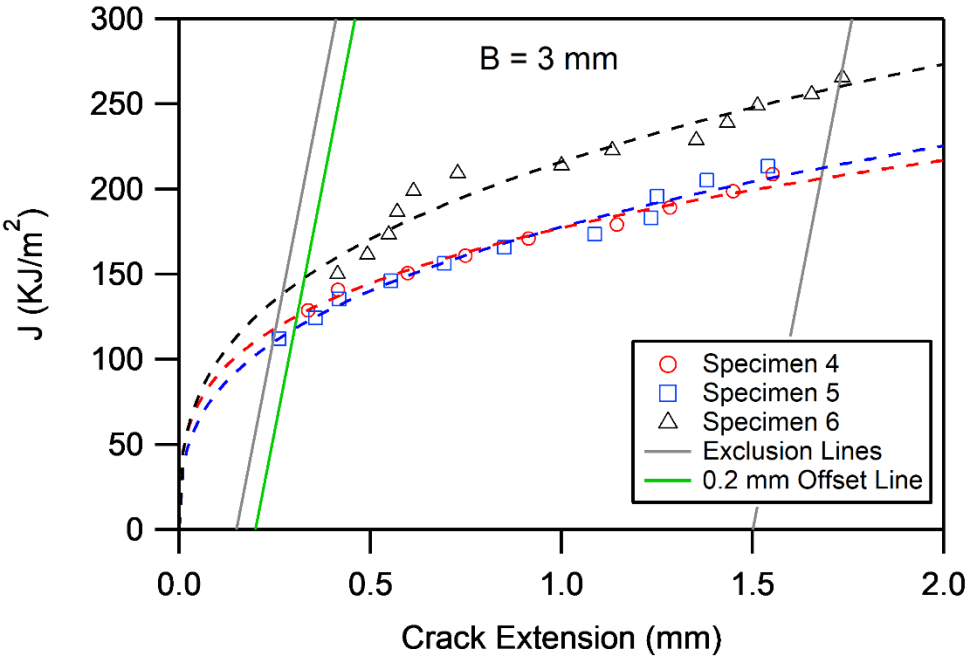
B = 3 mm
J (KJ/m^2)
Crack Extension (mm)
Specimen 4
Specimen 5
Specimen 6
Exclusion Lines
0.2 mm Offset Line
0
50
100
150
200
250
300
0.0
0.5
1.0
1.5
2.0

(c)

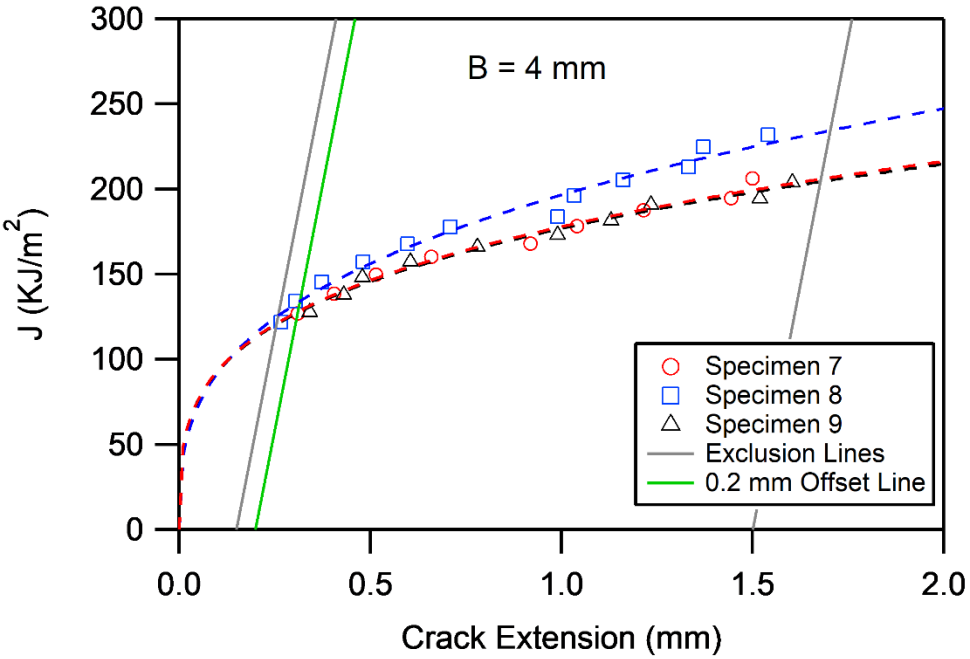

(d)

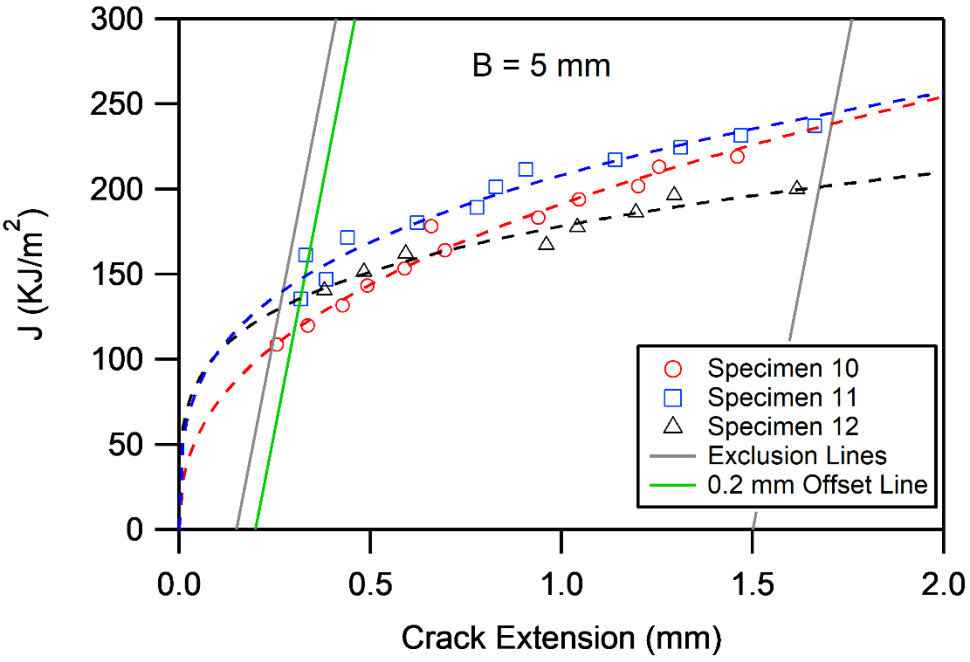

Figure 4.3. J-R curves for NiTi specimens with four different thickness values: (a) 2 mm, (b) 3 mm, (c) 4 mm, (d) 5 mm. J_{Ic} values are determined from the intersection point of 0.2mm offset line and the regression line.

Similarly, the resistance curves can be obtained for extrapolated stress intensity factor, $K_{J_{IC}}$, and the critical stress intensity factor, K_Q, (assuming LEFM is valid) for comparison. The K-R curves for K_J-values have a rising trend very similar to the resistance curves obtained with J-values, whereas the K-R curves for *K*-values are flat (see Figure 4.4). The apparent difference between the K_J, and K resistance curves comes from the inelastic behavior of the NiTi SMA specimens under mode-I fracture loading conditions.

(a)

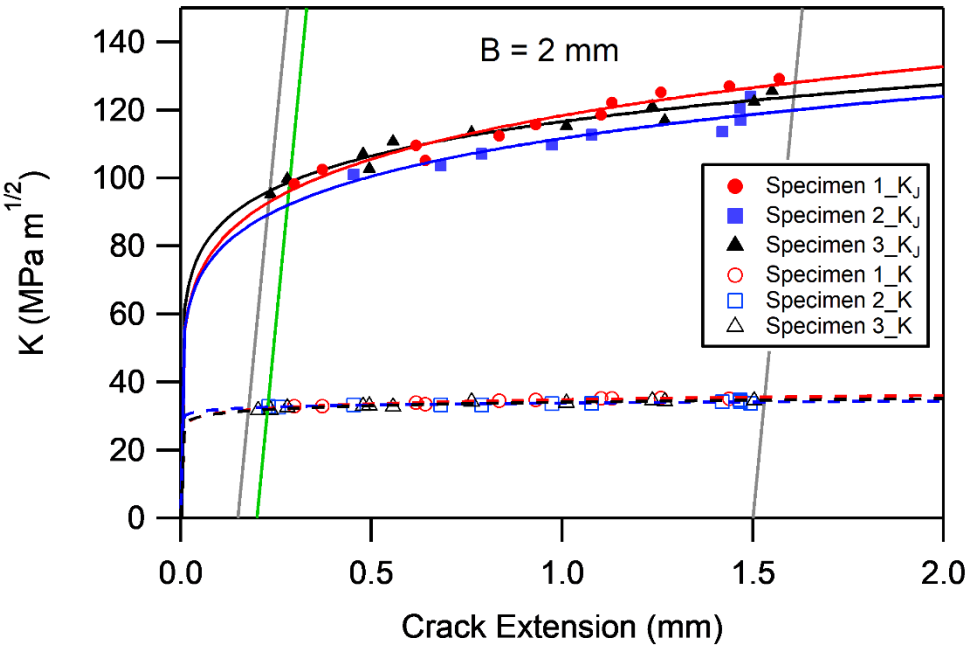

(b)

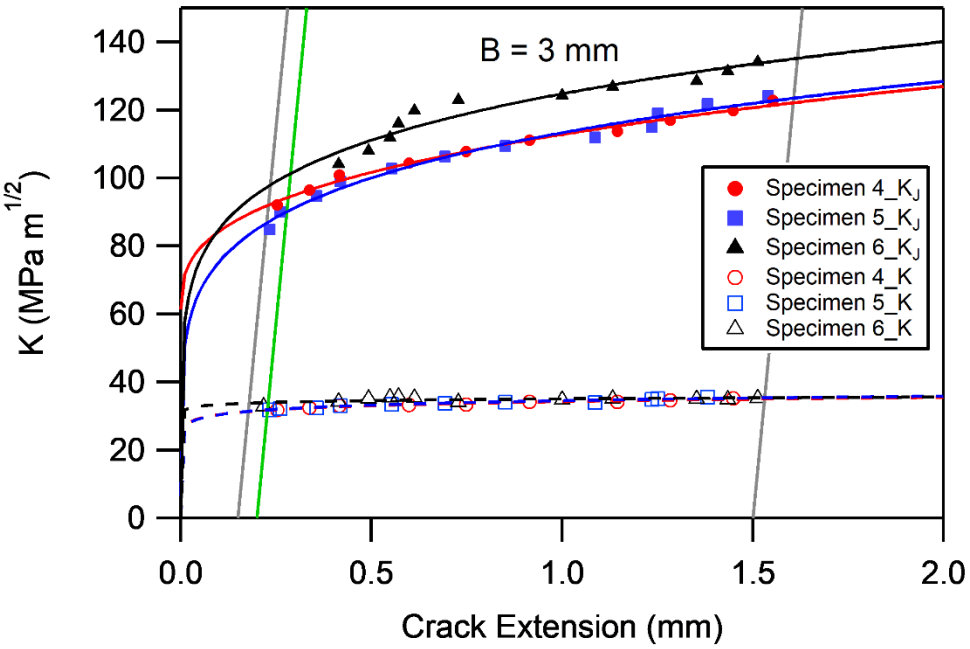
B = 3 mm
K (MPa m^1/2)
Crack Extension (mm)
Specimen 4_K_J
Specimen 5_K_J
Specimen 6_K_J
Specimen 4_K
Specimen 5_K
Specimen 6_K
0
20
40
60
80
100
120
140
0.0
0.5
1.0
1.5
2.0

(c)

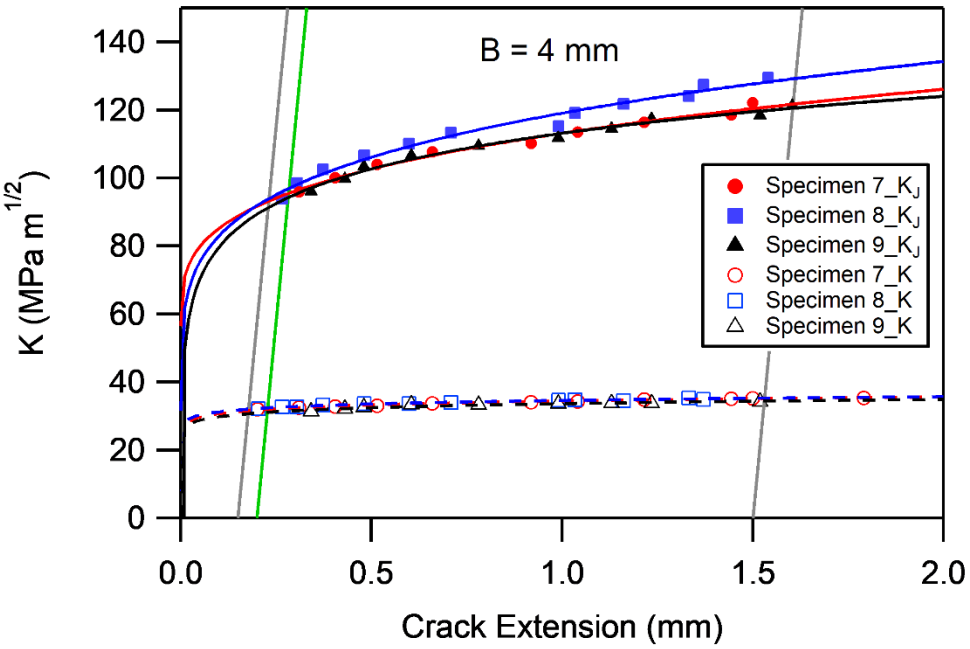
B = 4 mm
K (MPa m^1/2)
Crack Extension (mm)
Specimen 7_K_J
Specimen 8_K_J
Specimen 9_K_J
Specimen 7_K
Specimen 8_K
Specimen 9_K
0
20
40
60
80
100
120
140
0.0
0.5
1.0
1.5
2.0

(d)

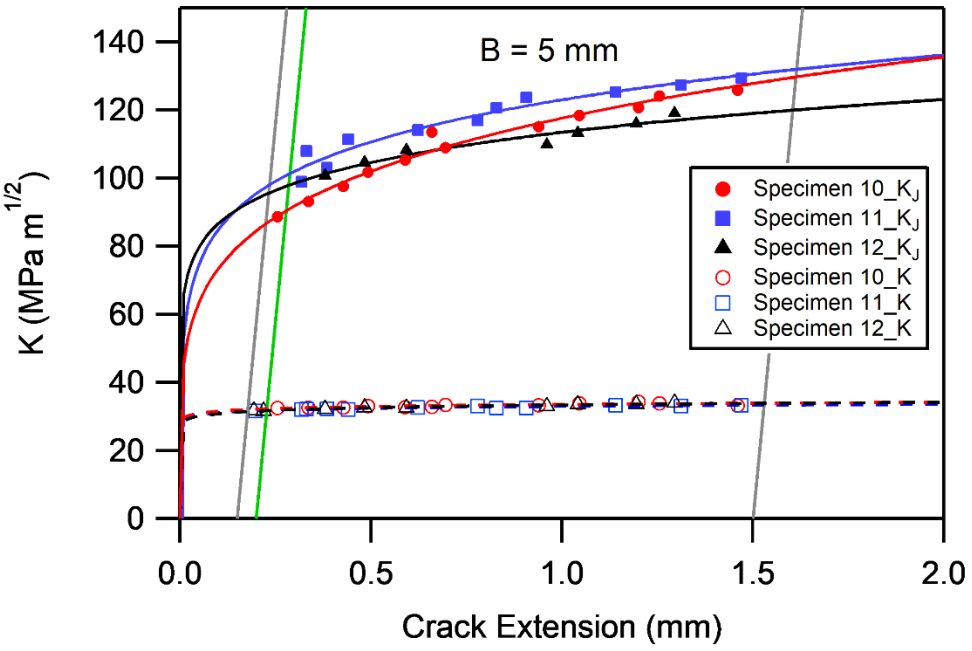

Figure 4.4. K-R curves for NiTi specimens with four different thickness values: (a) 2 mm, (b) 3 mm, (c) 4 mm, (d) 5 mm.

4.4. Fracture Toughness

The J_{Ic} values are given in Table 4.2 for NiTi specimens with four different thickness values from 2 mm to 5 mm. In Figure 4.5, the average J_{Ic} values and standard deviations for each thickness are presented. Depending on the data obtained from the experiments, no specific trend was observed, suggesting no thickness effect on fracture toughness in the thickness range investigated.

Table 4.2. J_{Ic} values for NiTi samples at different thickness values from 2mm to 5mm.

Nominal Thickness	Specimen #	J_{IC} [kJ/m^2]	Average J_{IC} [kJ/m^2]
2 mm	Specimen 1	132	130 ± 9
	Specimen 2	120	
	Specimen 3	139	
3 mm	Specimen 4	126	131 ± 15
	Specimen 5	118	
	Specimen 6	148	
4 mm	Specimen 7	128	130 ± 4
	Specimen 8	134	
	Specimen 9	127	
5 mm	Specimen 10	117	134 ± 16
	Specimen 11	149	
	Specimen 12	136	

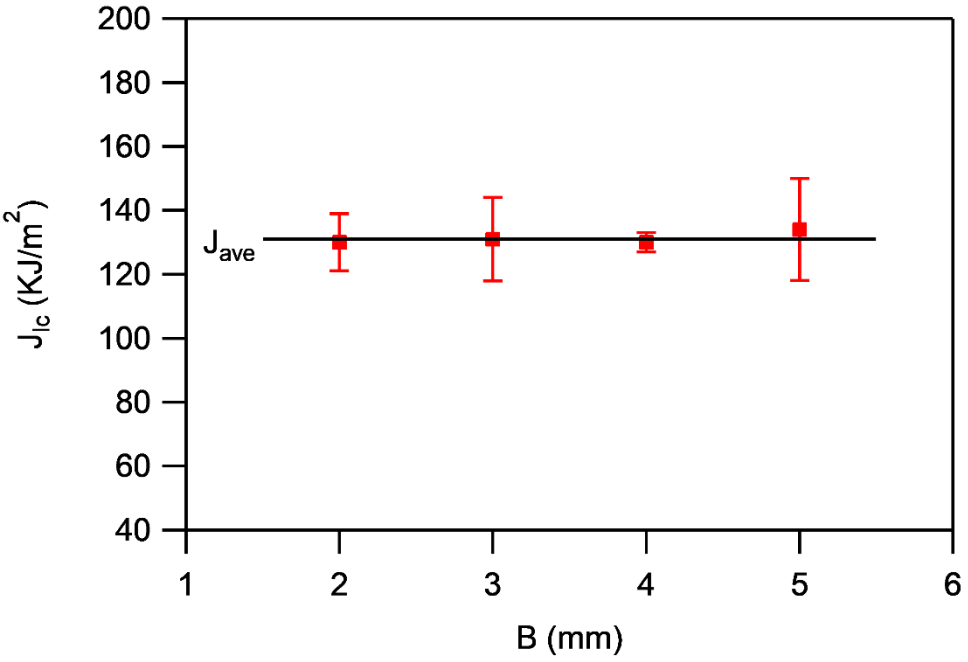

Figure 4.5 J_{Ic} values for NiTi samples having different thickness values from 2mm to 5mm

The extrapolated stress intensity factor, K_{JIc} can be determined with the following relation:

$$K_{JIc} = \sqrt{J_{Ic}E/(1-\nu^2)} \tag{15}$$

To compare the J-values with the stress intensity factor which was considered as the fracture toughness parameter in the majority of the studies for NiTi SMAs (assuming LEFM is valid), the following relation is used:

$$K_Q = \frac{P_Q}{B\sqrt{W}} f\left(\frac{a}{W}\right) \tag{16}$$

where $f\left(\frac{a}{W}\right)$ is the shape function and has the following form in ASTM E1820 [26]

$$f\left(\frac{a}{W}\right) = \frac{2+\left(\frac{a}{W}\right)\left[0.886+4.64\left(\frac{a}{W}\right)-13.32\left(\frac{a}{W}\right)^2+14.72\left(\frac{a}{W}\right)^3-5.6\left(\frac{a}{W}\right)^4\right]}{\left(1-\frac{a}{W}\right)^{\frac{3}{2}}}.$$

K_{JIC} and K_Q − values are summarized in Table 4.3.

Table 4.3. K_{JIc} and K_Q values for NiTi samples at different thickness values from 2 mm to 5 mm.

Nominal Thickness	$\boldsymbol{K_{J_{Ic}}}$**[MPa$\sqrt{\text{m}}$]**	$\boldsymbol{K_Q}$**[MPa$\sqrt{\text{m}}$]**
2 mm	96 ± 3	32 ± 1
3 mm	95 ± 5	33 ± 1
4 mm	96 ± 1	32 ± 1
5 mm	97 ± 6	32 ± 1

Similarly, the K_{JIC} and K_Q values are plotted together in Figure 4.6. Comparing the values given in Table 4.3, and plotted in Figure 4.6, one can see that the K_{JIC} and K_Q values are quite close for specimens with different thicknesses. Moreover, K_Q values are found to be consistent and very similar to the ones previously reported in the literature. Comparing the K-values, the fracture toughness results coming from the LEFM approach, K_Q, are found to be much less than the extrapolated K_{JIC} values derived from the J values which gives us that the LEFM approach is invalid.

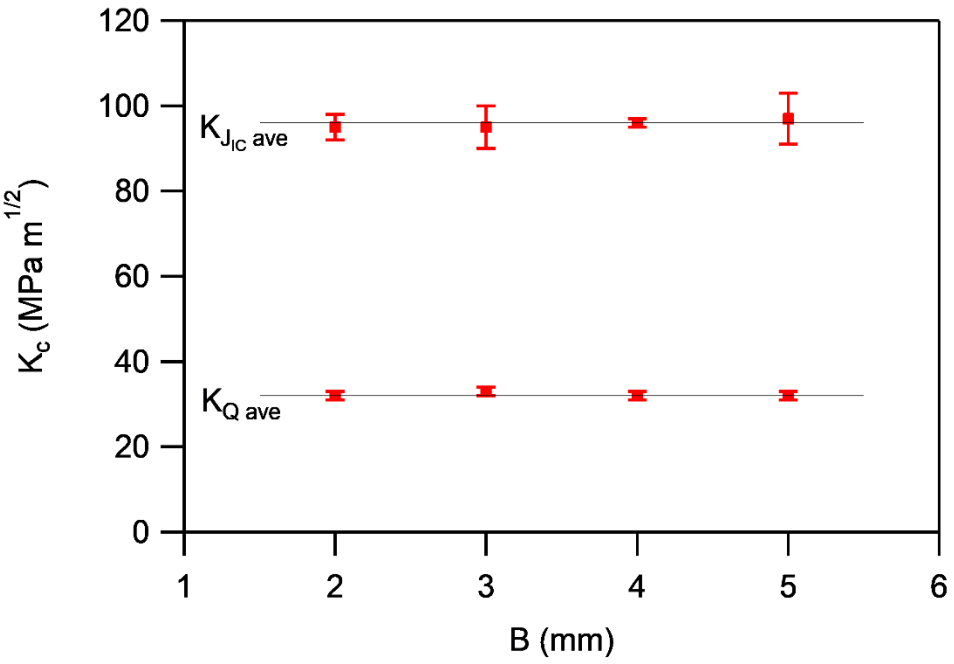

Figure 4.6. K_{JIc} and K_Q values for NiTi CT specimens with nominal thickness values from 2 mm to 5mm.

4.5. DIC Results

In this section, the progression of the strain fields in NiTi CT specimens with different thickness values subjected to mode-I loading is presented.

The strain fields are measured using the DIC method for all specimens at three directions; ε_{xx}, ε_{yy} and ε_{xy}. To be brief, the results are presented for the first set of specimens, i.e. one specimen is selected from each thickness value. Since the fracture experiments were conducted under displacement control, all reference points were selected in terms of load line displacements (LLD). The strain distributions are plotted at 0.5 mm, 1.0 mm, 1.5 mm, and 2.0 mm LLD points on the loading path, corresponding to average crack extensions of 0 mm (i.e. prior to crack growth), ~0.15 mm, ~0.75 mm, and ~1.5 mm, respectively. Figure 4.7 represents the load-displacement curves for the selected NiTi CT specimens with thickness values ranging from 2 mm to 5 mm. The dots on these curves give the load values at the specific displacement points which are the reference points for DIC images.

The strain field ε_{yy} representing the strain along the direction that is normal to the crack tip is plotted in Figure 4.8. For LLD = 0.5 mm, the deformation zone is quite small, limited to the very tip of the crack. As the LLD approaches to 1 mm, the deformation zone becomes larger forming the butterfly-like shape pointing in a direction of ~60° from the crack line.

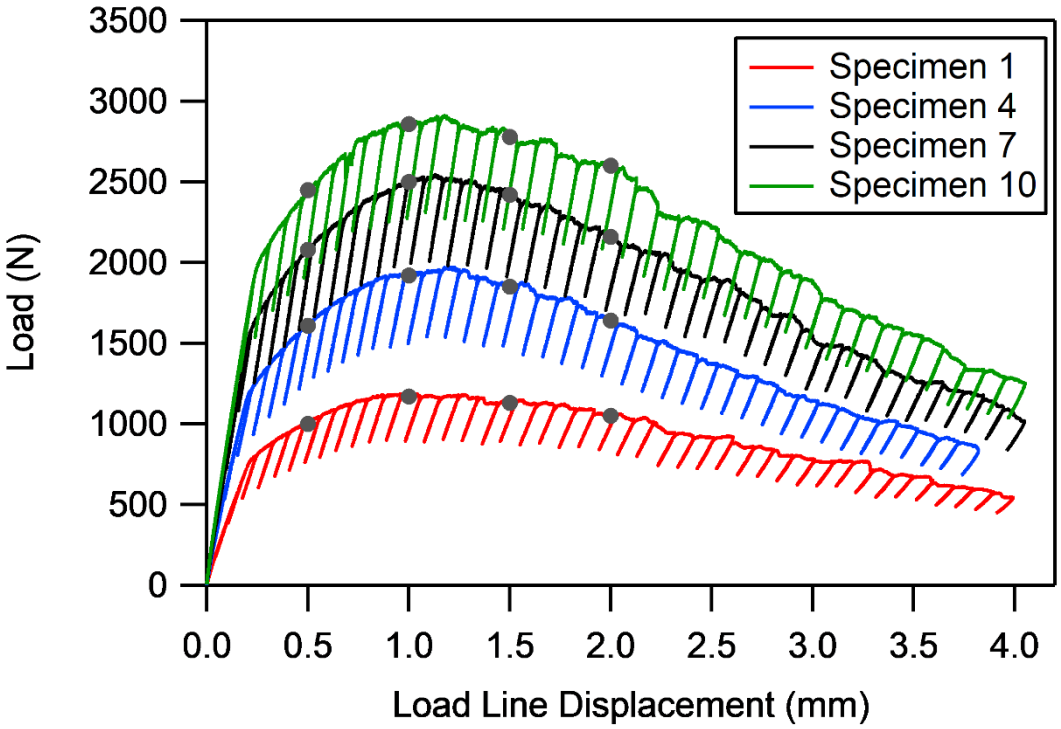

Figure 4.7. Load-displacement curves for NiTi CT specimens with thickness values 2-5 mm. The dots are the points for which the DIC results are provided at the selected load line displacements.

Regardless of the thickness of the specimen, the butterfly-like shape was observed in all CT specimens at sufficiently high loads. The two lobes of the butterfly-like shape grow notably but still keep the same form and orientation (pointing in a direction of ~60°) as the load increases. Moreover, the size and the shape of the lobes are very similar at the selected LLD reference points for different thickness values. The color selection of the contour was chosen so that the positive, negative, and around zero strain values are represented by red tones, purple-blue tones and green tones, respectively. Since the detwinning of the martensite was completed around 5% strain (as can be seen from Figure 4.1), the upper and lower limits of the scale was chosen accordingly. Therefore, the maximum strain value was reached at the crack tip of the specimen where the red zone

representing fully detwinned martensite in Figure 4.8. Going far from the crack tip, there was a decrease in the strain value. Moreover, at the very edge of the specimen negative strains with semi-circle shapes were observed due to compression.

The strain field along the direction of the crack extension (ε_{xx}) at 0.5 mm, 1.0 mm, 1.5 mm, and 2.0 mm applied displacement are plotted in Figure 4.9. For LLD = 0.5 mm, the deformation zone is quite small, limited to the very tip of the crack. As LLD approaches to 1 mm, the deformation zone becomes larger forming two butterfly-like shapes pointing in the directions of $\sim 60°$ and $\sim -60°$ from the crack tip, showing negative and positive strain values, respectively. Moreover, the shapes grow notably but still keep the same form and orientation as the load increases. The size and the shape of the lobes are observed to be very similar at the selected LLD reference points in all CT specimens regardless of the thickness.

The in-plane shear strain field (ε_{xy}) at 0.5 mm, 1.0 mm, 1.5 mm and 2.0 mm applied displacement are plotted in Figure 4.10. Similar to the previous results, the deformation zone is quite small for LLD = 0.5 mm. As the load increases, the deformation zone becomes larger forming two butterfly-like shapes, showing positive values at the 1st and 3rd quadrant, and negative values at the 2nd and 4th quadrant of the x-y plane. Regardless of the thickness, the size and the shape of the lobes are observed to be very similar at the selected LLD reference points in all CT specimens as the load continues to increase.

Considering the similarities between the contours of ε_{xx}, ε_{yy} and ε_{xy} plots, one may conclude that the specimen thickness has no significant effect on the mechanical

fields. It should be noted that because DIC is a surface measurement technique, the strain plots correspond to the surface of the specimens where the plane stress condition prevails. Therefore, drawing a conclusion based on the surface measurement may not represent the possible through-the-thickness variations.

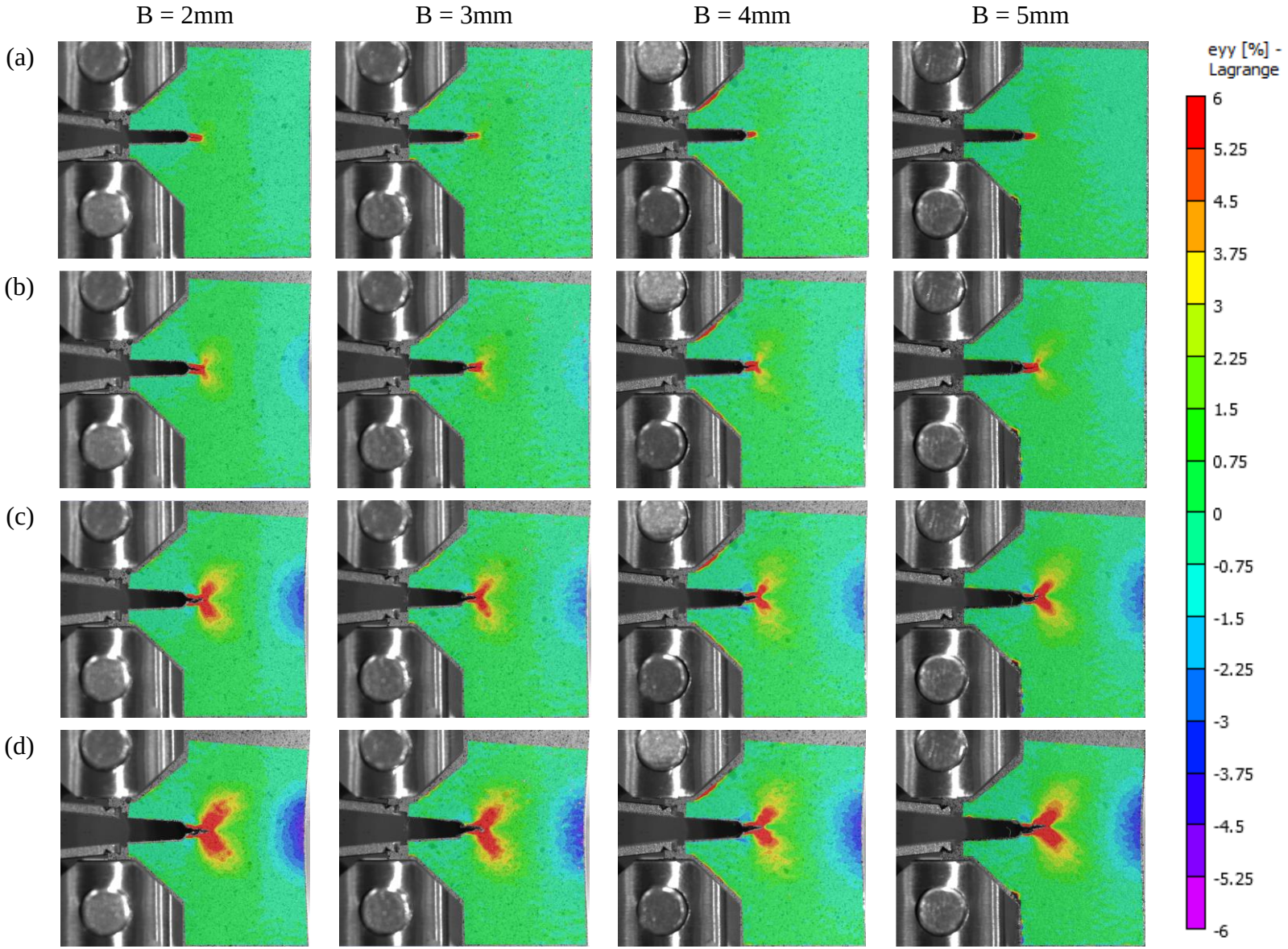

Figure 4.8. Strain distribution (ε_{yy}) for NiTi CT specimens obtained from DIC at LLD value of (a) 0.5 mm, (b) 1.0 mm, (c) 1.5 mm, (d) 2.0 mm.

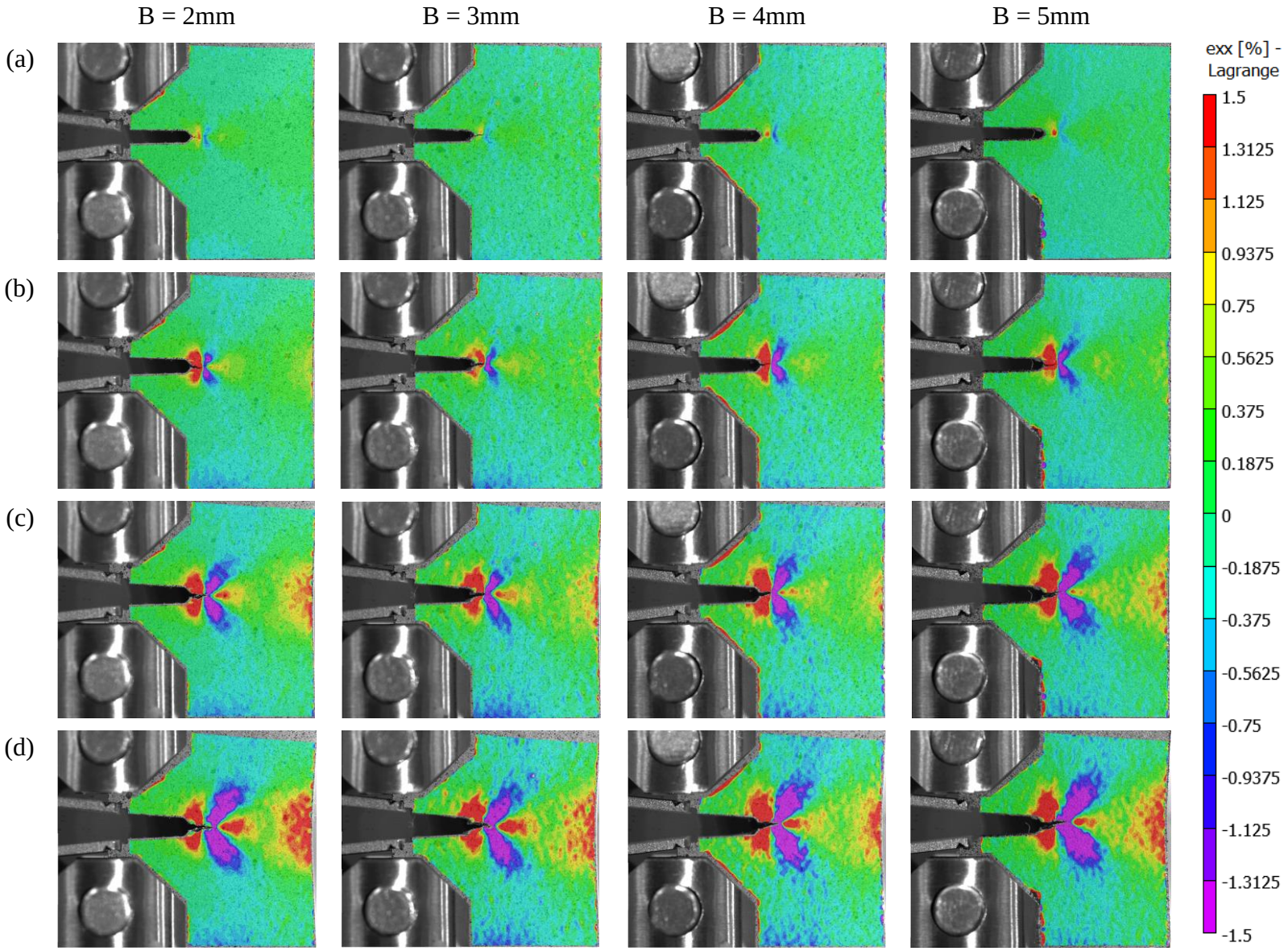

Figure 4.9. Strain distribution (ε_{xx}) for NiTi CT specimens obtained from DIC at LLD value of (a) 0.5 mm, (b) 1.0 mm, (c) 1.5 mm, (d) 2.0 mm.

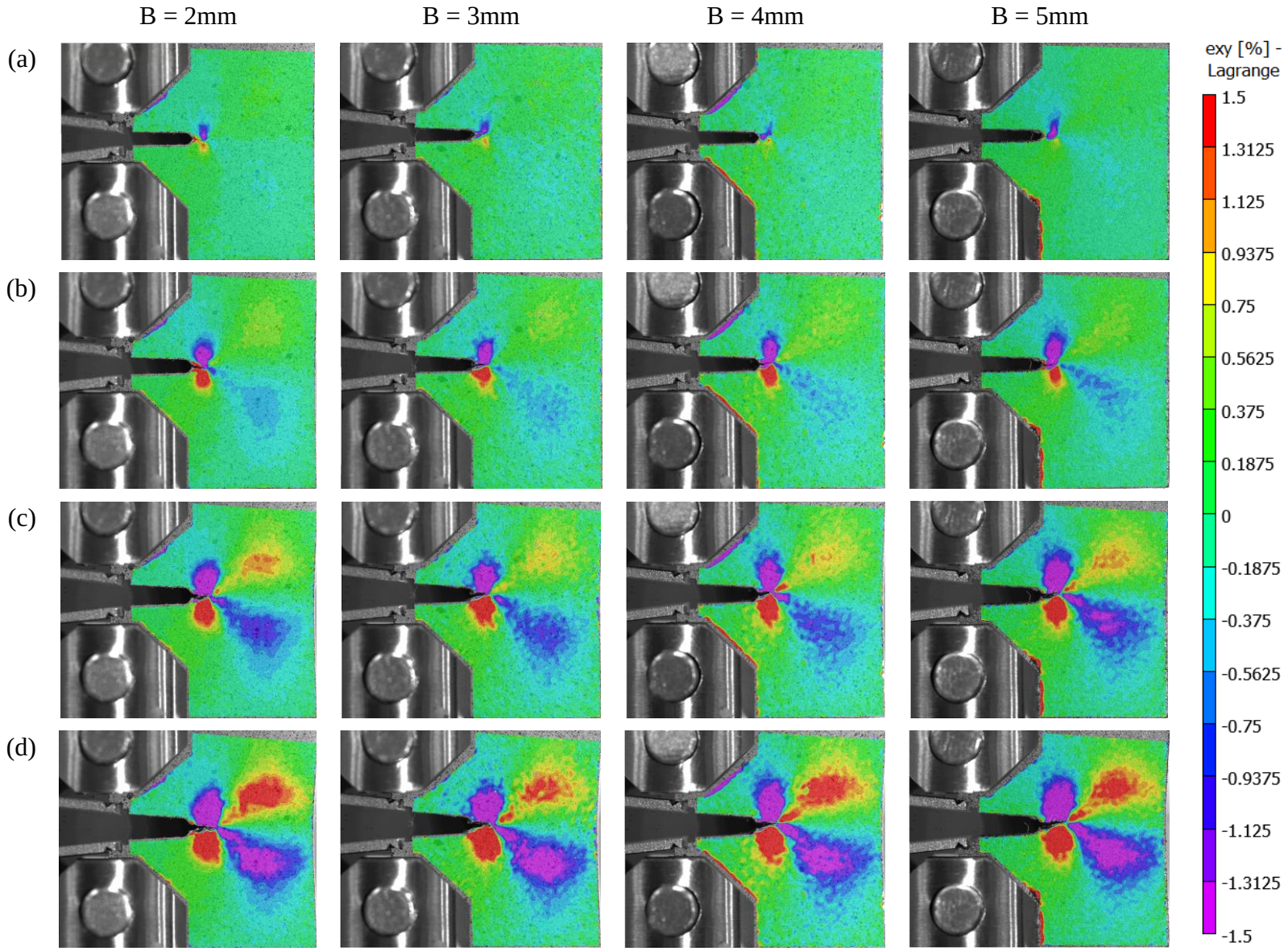

Figure 4.10. Strain distribution (ε_{xy}) for NiTi CT specimens obtained from DIC at LLD value of (a) 0.5 mm, (b) 1.0 mm, (c) 1.5 mm, (d) 2.0 mm.

4.6. Fracture Mechanism

The fracture surface was investigated using a scanning electron microscope (SEM). Figure 4.11.(a) is the SEM micrograph of the fracture surface of a 3 mm-thick NiTi CT specimen tested at room temperature. According to the figure, shear lip formation and crack tunneling were not observed in the low-magnification micrograph. Figure 4.11.(b) is the enlarged image of the fracture surface where cleavage fracture and ductile tearing were found to act in conjunction, resulting in a quasi-cleavage fracture surface. The decreasing trend of fracture toughness with increasing thickness is mainly a consequence of ductile fracture, i.e. void nucleation, growth, and coalescence. Therefore, the observation that the fracture toughness of NiTi doesn't follow this pattern is associated with the quasi-cleavage fracture mechanism.

According to the ASTM E1820 standard, the measured critical J value calculated from J-R curves is a size-independent value of fracture toughness to determine the fracture toughness if $b_0, B > 10\, J_{Ic}/\sigma_Y$, where σ_Y is the effective yield strength (the average of the ultimate tensile strength, σ^{TS}, and the critical stress, σ_{cr}). Using the material properties and the obtained critical J-integral values, to satisfy this condition the minimum required initial ligament and thickness is 2.3 mm. While all the specimens meet the initial ligament requirement, the 2 mm-thick specimens do not meet the thickness requirement. Considering the trend observed in this study, a new thickness requirement for SMAs, for which the fracture mechanics and mechanisms are unique compared to conventional metals, is desired.

(a)

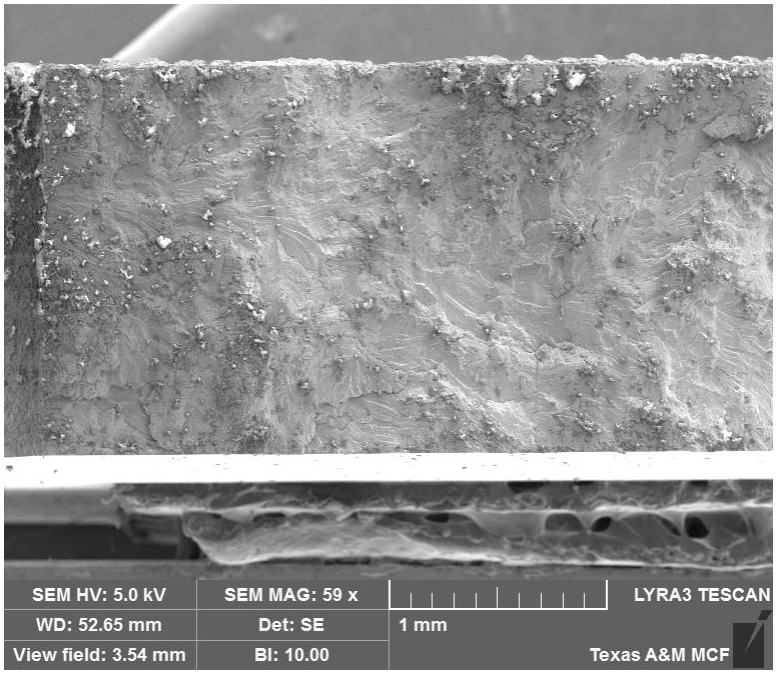

(b)

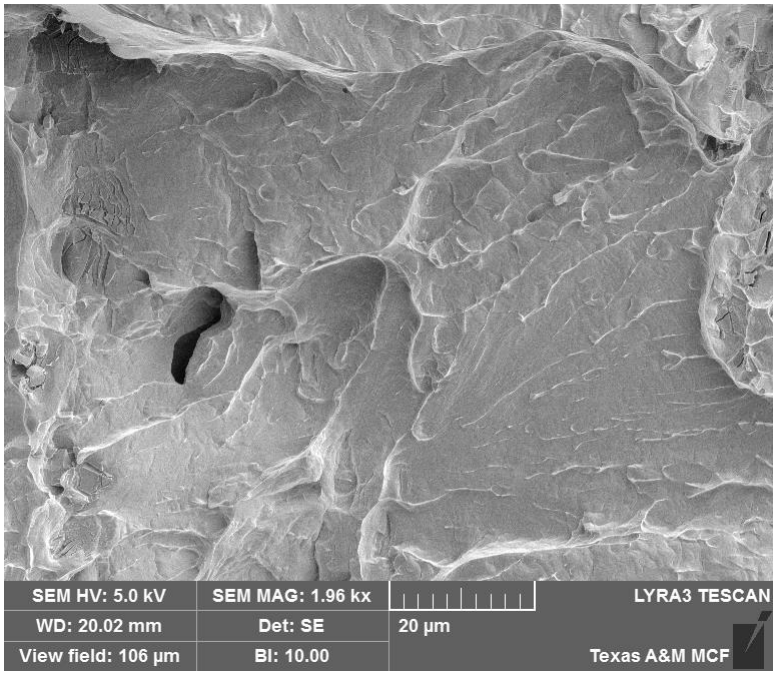

Figure 4.11. SEM images of the fracture surface from a 3 mm-thick compact tension specimen: a) low-magnification image showing no evidence of shear lips or crack tunneling, b) high-magnification image showing quasi-cleavage fracture mechanism.

5. CONCLUSIONS AND FUTURE WORK

The effect of thickness on fracture toughness of equiatomic NiTi SMA was investigated experimentally. Mode-I fracture experiments were conducted on NiTi compact tension specimens with four different thickness values (from 1 mm to 5 mm) at room temperature, at which martensite undergoes detwinning upon loading. In order to satisfy the repeatability of the obtained results, three sets of specimens (a total of 15 specimens) were used in the experiments. The load-displacements curves were plotted and the resistance curves were obtained using J-integral as the fracture parameter. J-values were calculated using a recently proposed methodology for SMAs that takes into account the apparent change in elastic modulus. Comparing the critical J-values showed no thickness effect for the thickness values investigated in this work. This is attributed to the underlying fracture mechanism in SMAs being dominated by cleavage with no evidence of shear lip formation or crack tunneling.

Resistance curves were also developed using extrapolated stress intensity factor, K_J, and were compared with those using the stress intensity factor, K, (assuming LEFM is valid) Rising R-curves were obtained for K_J values, whereas the resistance curves for K values were found to be flat. The fracture toughness values obtained from the LEFM approach were found to be very small compared to the extrapolated values, showing that the LEFM approach is not valid for SMAs where non-linear deformation region at the crack tip is large compared to the specimen dimensions.

The strain fields were characterized using digital image correlation and strain maps in three directions (ε_{xx}, ε_{yy} and ε_{xy}) were obtained. Evaluating the zone of nonlinear deformation mechanism, in this case detwinning, near the crack tip revealed no thickness effect on the surface of the specimen, where plane stress condition prevails.

Future studies that can further the knowledge on the effect of thickness on the fracture of SMAs are discussed below.

In this work, the experiments were conducted on SMA samples at room temperature (below M_f) at which the twinned martensite experiences detwinning upon loading. One can also compare the response of SMA samples at different temperatures so that besides martensitic, transforming (above A_f) and austenitic (above M_d) materials can also be tested. The phase transformation is a critical characteristic of SMAs, therefore, the thickness effect in SMAs undergoing phase transformation should be investigated. Moreover, phase transformation occurring during actuation loading (i.e. thermal cycling under constant load) may result in crack growth. Therefore, the thickness effect on the fracture of SMAs under thermal actuation can be investigated.

The SMA considered in this study (NiTi) showed stable crack growth. Therefore, other materials systems exhibiting unstable crack growth, such as NiTiHf SMAs, should be investigated. Furthermore, the effect of microstructure on thickness dependence of fracture toughness is yet to be studied.

Finally, in the present study, mode-I fracture experiments were conducted. Thickness effect on fracture of SMAs under other modes of loading, or a combination of two or three modes (mixed-mode) can be investigated. This is important for SMA applications such as torque tubes where the SMA component may experience complex loading conditions.

REFERENCES

1. Lagoudas, D.C., *Shape memory alloys: modeling and engineering applications*. 2008: Springer.
2. Baxevanis, T. and D. Lagoudas, *Fracture mechanics of shape memory alloys: review and perspectives.* International Journal of Fracture, 2015. **191**(1-2): p. 191-213.
3. Robertson, S., A. Mehta, A. Pelton, and R. Ritchie, *Evolution of crack-tip transformation zones in superelastic Nitinol subjected to in situ fatigue: A fracture mechanics and synchrotron X-ray microdiffraction analysis.* Acta Materialia, 2007. **55**(18): p. 6198-6207.
4. Creuziger, A., L. Bartol, K. Gall, and W. Crone, *Fracture in single crystal NiTi.* Journal of the Mechanics and Physics of Solids, 2008. **56**(9): p. 2896-2905.
5. Gollerthan, S., M. Young, K. Neuking, U. Ramamurty, and G. Eggeler, *Direct physical evidence for the back-transformation of stress-induced martensite in the vicinity of cracks in pseudoelastic NiTi shape memory alloys.* Acta materialia, 2009. **57**(19): p. 5892-5897.
6. Holtz, R., K. Sadananda, and M. Imam, *Fatigue thresholds of Ni-Ti alloy near the shape memory transition temperature.* International Journal of Fatigue, 1999. **21**: p. S137-S145.
7. Robertson, S.W. and R.O. Ritchie, *In vitro fatigue–crack growth and fracture toughness behavior of thin-walled superelastic Nitinol tube for endovascular stents: A basis for defining the effect of crack-like defects.* Biomaterials, 2007. **28**(4): p. 700-709.
8. Daly, S., A. Miller, G. Ravichandran, and K. Bhattacharya, *An experimental investigation of crack initiation in thin sheets of nitinol.* Acta Materialia, 2007. **55**(18): p. 6322-6330.
9. Gollerthan, S., M. Young, A. Baruj, J. Frenzel, W.W. Schmahl, and G. Eggeler, *Fracture mechanics and microstructure in NiTi shape memory alloys.* Acta Materialia, 2009. **57**(4): p. 1015-1025.
10. Maletta, C., E. Sgambitterra, and F. Furgiuele, *Crack tip stress distribution and stress intensity factor in shape memory alloys.* Fatigue & Fracture of Engineering Materials & Structures, 2013. **36**(9): p. 903-912.
11. Ahadi, A. and Q. Sun, *Grain size dependence of fracture toughness and crack-growth resistance of superelastic NiTi.* Scripta Materialia, 2016. **113**: p. 171-175.

12. Katanchi, B., N. Choupani, J. Khalil-Allafi, R. Tavangar, and M. Baghani, *Mixed-mode fracture of a superelastic NiTi alloy: Experimental and numerical investigations.* Engineering Fracture Mechanics, 2018. **190**: p. 273-287.

13. Iliopoulos, A., J. Steuben, T. Kirk, T. Baxevanis, J. Michopoulos, and D. Lagoudas, *Thermomechanical failure response of notched NiTi coupons.* International Journal of Solids and Structures, 2017. **125**: p. 265-275.

14. Robertson, S., A. Pelton, and R. Ritchie, *Mechanical fatigue and fracture of Nitinol.* International Materials Reviews, 2012. **57**(1): p. 1-37.

15. Maletta, C., E. Sgambitterra, and F. Niccoli, *Temperature dependent fracture properties of shape memory alloys: novel findings and a comprehensive model.* Scientific reports, 2016. **6**(1): p. 17.

16. Luo, J., J. He, X. Wan, T. Dong, Y. Cui, and X. Xiong, *Fracture properties of polycrystalline NiTi shape memory alloy.* Materials Science Engineering: A, 2016. **653**: p. 122-128.

17. Vaidyanathan, R., D. Dunand, and U. Ramamurty, *Fatigue crack-growth in shape-memory NiTi and NiTi–TiC composites.* Materials Science Engineering: A, 2000. **289**(1-2): p. 208-216.

18. Robertson, S. and R. Ritchie, *A fracture-mechanics-based approach to fracture control in biomedical devices manufactured from superelastic Nitinol tube.* Journal of Biomedical Materials Research Part B: Applied Biomaterials, 2008. **84**(1): p. 26-33.

19. Ramaiah, K., C. Saikrishna, V. Ranganath, V. Buravalla, and S. Bhaumik, *Fracture of thermally activated NiTi shape memory alloy wires.* Materials Science and Engineering: A, 2011. **528**(16-17): p. 5502-5510.

20. Haghgouyan, B., C. Hayrettin, T. Baxevanis, I. Karaman, and D.C. Lagoudas, *Fracture toughness of niti–towards establishing standard test methods for phase transforming materials.* Acta Materialia, 2019. **162**: p. 226-238.

21. Gollerthan, S., D. Herberg, A. Baruj, and G. Eggeler, *Compact tension testing of martensitic/pseudoplastic NiTi shape memory alloys.* Materials Science and Engineering: A, 2008. **481**: p. 156-159.

22. Haghgouyan, B., N. Shafaghi, C.C. Aydıner, and G. Anlas, *Experimental and computational investigation of the effect of phase transformation on fracture parameters of an SMA.* Smart materials and structures, 2016. **25**(7): p. 075010.

23. Haghgouyan, B., S. Jape, C. Hayrettin, T. Baxevanis, I. Karaman, and D.C. Lagoudas. *Experimental and numerical investigation of the stable crack growth regime under pseudoelastic loading in shape memory alloys*. in *Behavior and Mechanics of Multifunctional Materials and Composites XII*. 2018. International Society for Optics and Photonics.

24. Standard, A., *E399.* Standard Test Method for Linear-Elastic Plane-Strain Fracture Toughness KIC of Metallic Materials," in ASTM Book of Standards, West Conshohocken, PA: ASTM International, 2012.

25. Anderson, T.L., *Fracture mechanics: fundamentals and applications*. 2017: CRC press.

26. Testing, A.S.f. and Materials, *ASTM E1820: standard test method for measurement of fracture toughness*. 2015, ASTM International West Conshohocken.

27. He, J., K. Gao, Y. Su, L. Qiao, and W. Chu, *The role of hydride, martensite and atomic hydrogen in hydrogen-induced delayed fracture of TiNi alloy.* Materials Science and Engineering: A, 2004. **364**(1-2): p. 333-338.

28. Hartl, D., B. Volk, D.C. Lagoudas, F. Calkins, and J. Mabe. *Thermomechanical Characterization and Modeling of Ni60Ti40 SMA for Actuated Chevrons*. in *ASME 2006 International Mechanical Engineering Congress and Exposition*. 2006.

29. Oehler, S., D. Hartl, R. Lopez, R. Malak, and D. Lagoudas, *Design optimization and uncertainty analysis of SMA morphing structures.* Smart Materials and Structures, 2012. **21**(9): p. 094016.

30. Calkins, F.T. and J.H. Mabe, *Shape Memory Alloy Based Morphing Aerostructures.* Journal of Mechanical Design, 2010. **132**(11).

31. Mabe, J., F. Calkins, and G. Butler. *Boeing's variable geometry chevron, morphing aerostructure for jet noise reduction*. in *47th AIAA/ASME/ASCE/AHS/ASC Structures, Structural Dynamics, and Materials Conference 14th AIAA/ASME/AHS Adaptive Structures Conference 7th*. 2006.

32. Brown, W.F. and J.E. Srawley, *Plane strain crack toughness testing of high strength metallic materials*. Vol. 410. 1967: American Society for Testing and Metarials.

33. Makkar, J. and T. Baxevanis, *Notes on the experimental measurement of fracture toughness of shape memory alloys.* Journal of Intelligent Material Systems and Structures, 2020. **31**(3): p. 475-483.

34. Gall, K., N. Yang, H. Sehitoglu, and Y.I. Chumlyakov, *Fracture of precipitated NiTi shape memory alloys.* International journal of fracture, 2001. **109**(2): p. 189-207.

35. Rolfe, S.T. and J.M. Barsom, *Fracture and fatigue control in structures: Applications of fracture mechanics(Book).* Englewood Cliffs, N. J., Prentice-Hall, Inc., 1977. 574 p, 1977.

36. Rice, J.R., *A path independent integral and the approximate analysis of strain concentration by notches and cracks.* 1968.

37. Irwin, G.R., *Analysis of stresses and strains near the end of a crack transversing a plate.* Trans. ASME, Ser. E, J. Appl. Mech., 1957. **24**: p. 361-364.

38. Zhu, X.-K. and J.A. Joyce, *Review of fracture toughness (G, K, J, CTOD, CTOA) testing and standardization.* Engineering Fracture Mechanics, 2012. **85**: p. 1-46.

39. Begley, J. and J. Landes, *The J integral as a fracture criterion*, in *Fracture toughness: part II*. 1972, ASTM International.

40. Landes, D. and J. Begley, *The effect of specimen geometry on J Ic*, in *Fracture Toughness: Part II*. 1972, ASTM International.

41. Rice, J., P. Paris, and J. Merkle, *Some further results of J-integral analysis and estimates*, in *Progress in flaw growth and fracture toughness testing*. 1973, ASTM International.

42. Landes, J., H. Walker, and G. Clarke, *Evaluation of Estimation Procedures used in J-lntegral Testing*, in *Elastic-plastic fracture*. 1979, ASTM International.

43. Griffith, A.A., *VI. The phenomena of rupture and flow in solids.* Philosophical transactions of the royal society of london. Series A, containing papers of a mathematical or physical character, 1921. **221**(582-593): p. 163-198.

44. Ernst, H., P. Paris, and J. Landes, *Estimations on J-integral and tearing modulus T from a single specimen test record*, in *Fracture mechanics*. 1981, ASTM International.

45. Saxena, A. and C.L. Muhlstein, *Fatigue Crack Growth Testing*, in *Fatigue and Fracture*. 1996, ASM International. p. 0.

46. Clarke, G., W. Andrews, P. Paris, and D. Schmidt, *Single specimen tests for J Ic determination*, in *Mechanics of crack growth*. 1976, ASTM International.

47. Joyce, J. and J. Gudas, *Computer interactive J Ic of testing navy alloys*, in *Elastic-plastic fracture*. 1979, ASTM International.

48. Saxena, A. and S. Hudak, *Review and extension of compliance information for common crack growth specimens.* International Journal of Fracture, 1978. **14**(5): p. 453-468.

49. Schreier, H., J.-J. Orteu, and M.A. Sutton, *Image correlation for shape, motion and deformation measurements: Basic concepts, theory and applications*. Vol. 1. 2009: Springer.

50. Rice, J., P. Paris, and J. Merkle, *Progress in flaw growth and fracture toughness testing.* ASTM STP, 1973. **536**: p. 231-245.

51. Merkle, J. and H. Corten, *AJ integral analysis for the compact specimen, considering axial force as well as bending effects.* 1974.

52. Paris, P.C., H. Ernst, and C. Turner, *A J-integral approach to development of η-factors*, in *Fracture Mechanics*. 1980, ASTM International.

53. Clarke, G. and J. Landes, *Evaluation of the J integral for the compact specimen.* Journal of Testing and Evaluation, 1979. **7**(5): p. 264-269.

APPENDIX A

SPECIMEN THICKNESS REQUIREMENT FOR SMAS

This appendix discusses the need for modification to ASTM standard, regarding the specimen thickness requirement to ensure a thickness-independent fracture toughness measurement. As mentioned in Section 1.2, to comply with the small-scale yielding condition, which is a prerequisite for measuring the critical stress intensity factor (K_{Ic}) in conventional materials, the following size requirement should be met

$$B > 2.5\left(\frac{K_{Ic}}{\sigma_y}\right)^2.$$

In this equation, B is the specimen thickness, and σ_y is the yield stress. In the case of SMAs, σ_y should be interpreted as the stress required for the stress-induced transformation/detwinning, not the yield stress. In other words, for LEFM to be valid, the zone of nonlinear deformation, regardless of the mechanism, should be small compared to the thickness of the specimen. For such a requirement to be satisfied, the SMA specimens need to be prohibitively large. For instance, using the material properties obtained in this study, the required minimum thickness to satisfy the aforementioned criterion is ~62 mm. Therefore, as proposed in a recent study [20], the fracture toughness of SMAs should be measured using J-integral as the fracture criterion, for which the requirements on specimen size are much less strict compared to those for valid K_{Ic} measurement.

According to ASTM E1820 [26], the measured interim critical J value obtained from a resistance curve is a thickness-independent value of fracture toughness if the following requirement is met

$$B > 10\,\frac{J_{Ic}}{\sigma_Y},$$

where σ_Y is the effective yield strength, i.e. the average of the ultimate tensile strength, σ^{TS}, and the yield stress σ_y. For SMAs, σ_y should be replaced by σ_{cr} which denotes the stress required for either transformation, detwinning, or austenite yield, depending on the ambient temperature. Although some of the specimens tested in this study had thickness values below the ASTM requirement, they did not exhibit a thickness dependence, indicating that the thickness requirement may be severe for SMAs.

The thickness dependence of fracture toughness in metals corresponds to those where the crack propagation mechanism is ductile, i.e. void nucleation, growth and coalescence. In such materials, crack tunneling occurs through the center of the specimen where the triaxiality is higher, and the fracture surface shows a flat region in the middle and shear lips on the edges [25]. Although SMAs show highly nonlinear response, they fail predominantly by cleavage fracture. As shown in this study, crack tunneling and shear lips were not evident on the cleavage-dominated fracture surface. This suggests that compared to conventional ductile metals, the fracture toughness in SMAs is less sensitive to the specimen thickness, and hence, the ASTM thickness requirement to ensure a constrain-independent fracture toughness measurement is stringent for SMAs, the deformation, and fracture mechanism of which differs from those of conventional metals.

APPENDIX B

DETERMINATION OF GEOMETRY FACTORS

To develop η-factors, a J-integral approach will be used with the following form

$$J = -\int \frac{\partial \mathrm{P}}{\partial \mathrm{a}} d\delta = \int \frac{\partial \delta}{\partial \mathrm{a}} dP \tag{B.1}$$

where P is the load per unit thickness and δ is the load point displacement. When we split the displacement into its elastic and inelastic components,

$$\delta = \delta^{el} + \delta^{in} \tag{B.2}$$

J-integral will also be separated into elastic and inelastic components as follows:

$$J = J^{el} + J^{in} = -\int_0^{\delta^{el}} \frac{\partial \mathrm{P}}{\partial \mathrm{a}}\Big|_{\delta^{el}} d\delta^{el} - \int_0^{\delta^{in}} \frac{\partial \mathrm{P}}{\partial \mathrm{a}}\Big|_{\delta^{in}} d\delta^{in} \tag{B.3}$$

B.1. Elastic η-factor

The linear elastic displacement, δ^{el}, can be approximated as

$$\delta = C \cdot P \tag{B.4}$$

where C is the elastic compliance and can be measured from the slope of each unloading curve of the load-displacement data. Moreover, the elastic part of the J integral can be written in terms of $\partial \mathrm{C}/\partial \mathrm{a}$ as follows

$$J^{el} = -\int_0^{\delta^{el}} \frac{\partial \mathrm{P}}{\partial \mathrm{a}}\Big|_{\delta^{el}} d\delta^{el} = \frac{1}{C}\frac{\partial \mathrm{C}}{\partial \mathrm{a}} \int_0^{\delta^{el}} P \, d\delta^{el} \tag{B.5}$$

Using the relation

$$\int_0^{\delta^{el}} P \, d\delta^{el} = \frac{A^{el}}{B} \tag{B.6}$$

The elastic component of the J-integral becomes

$$J^{el} = \frac{1}{C}\frac{\partial \mathrm{C}}{\partial \mathrm{a}}\frac{A^{el}}{B} \tag{B.7}$$

From the foreknown equation of J^{el}

$$J^{el} = \eta^{el}\frac{A^{el}}{Bb} \tag{B.8}$$

The elastic component of η-factor comes out to be

$$\eta^{el} = \frac{b}{C}\frac{\partial \mathrm{C}}{\partial \mathrm{a}} \tag{B.9}$$

With this approximation it becomes apparent that the change in the area under the load-displacement curve influences the elastic properties of the material, therefore, influences both the elastic and inelastic components of the J-integral.

B.2. Inelastic η-factor

Referring to the last term of equation (B.3), J^{in}; the load, P, can be written as a function of crack size, a, inelastic component of the displacement, δ^{in}, and other dimensional terms such as L, B, W, etc., where L, B and W are length, thickness and width of the specimen, respectively, leading to

$$\frac{P}{W} = F_1\left(\frac{\delta^{in}}{W}, \frac{a}{W}, \frac{L}{W}, \frac{B}{W}, \ldots\ldots, etc\right) \tag{B.10}$$

Or alternatively use the remaining unbroken ligament, b, and factor out by $(b/W)^2$

$$P = \frac{b^2}{W}F_2\left(\frac{\delta^{in}}{W}, \frac{a}{W}, \frac{L}{W}, \frac{B}{W}, \ldots\ldots, etc\right) \tag{B.11}$$

Substitute equation (B.11) into equation (B.1) and use the relation $db = -da$

$$J^{in} = -\int_0^{\delta^{in}} \frac{\partial \mathrm{P}}{\partial \mathrm{a}}\Big|_{\delta^{in}} d\delta^{in} = \frac{2b}{W}\int_0^{\delta^{in}} F d\delta^{in} - \frac{b^2}{W^2}\int_0^{\delta^{in}} \frac{\partial \mathrm{F}}{\partial\left(\frac{a}{W}\right)} d\delta^{in} \tag{B.12}$$

The first term of equation (B.12) is the area under the load-displacement curve with a $2/b$ coefficient as stated in Rice [50], and the second term comes from Merkle-Corten [51].

The inelastic component of η-factor can be defined in a manner very similar to its elastic counterpart given in equation (B.8) in the following form:

$$J^{in} = \eta^{in}\frac{A^{in}}{Bb} \tag{B.13}$$

Moreover, the inelastic component of η-factor can exist when crack length and plastic displacement dependencies are separated as follows

$$F\left(\frac{\delta^{in}}{W}, \frac{a}{W}, \ldots\ldots, etc\right) = G\left(\frac{\delta^{in}}{W}, \ldots\ldots, etc\right) \cdot H\left(\frac{a}{W}, \ldots\ldots, etc\right) \tag{B.14}$$

Then it will become

$$\begin{aligned}\int_0^{\delta^{in}} \frac{\partial \mathrm{F}}{\partial\left(\frac{a}{W}\right)} d\delta^{in} &= \frac{\partial \mathrm{H}}{\partial\left(\frac{a}{W}\right)}\int_0^{\delta^{in}} G d\delta^{in} \\ &= \frac{\partial \mathrm{H}}{\partial\left(\frac{a}{W}\right)}\frac{1}{H}\int_0^{\delta^{in}} F d\delta^{in} \\ &= \frac{\partial \mathrm{H}}{\partial\left(\frac{a}{W}\right)}\frac{W}{b^2 H}\int_0^{\delta^{in}} P d\delta^{in}\end{aligned} \tag{B.15}$$

Substitute equation (B.15) into equation (B.12), the inelastic component of J-integral will be

$$J^{in} = \frac{1}{b}\int_0^{\delta^{in}} P d\delta^{in}\left[2 - \frac{b}{W}\frac{\partial \mathrm{H}}{\partial\left(\frac{a}{W}\right)}\frac{1}{H}\right] \tag{B.16}$$

Therefore, the inelastic component of η-factor will be

$$\eta^{in} = 2 - \frac{b}{W}\frac{\partial \mathrm{H}}{\partial\left(\frac{a}{W}\right)}\frac{1}{H} \tag{B.17}$$

where $\int_0^{\delta^{in}} P d\delta^{in} = \frac{A^{in}}{B}$

In order to satisfy the condition for η^{in} existence, Paris et al. [52] suggested a power hardening material, characterized by

$$\frac{\epsilon}{\epsilon_0} = \left(\frac{\sigma}{\sigma_0}\right)^N \tag{B.18}$$

where $N \to 1$ for the nearly elastic behavior.

Clarke and Landes [53] proposed the following expression for the inelastic component of η-factor for CT specimen which is a good approximation for SMAs.

$$\eta^{in} = 2 + 0.522\left(\frac{b}{W}\right) \tag{B.19}$$

APPENDIX C

RESULTS FOR 1 MM THICK CT SPECIMEN

C.1. Load-Displacement Data

The experimental load-displacement data for NiTi CT specimen having 1mm thickness from Test 1 and Test 2 is given in Figure C.1. As the load increases, the specimen started to buckle around 1 mm of crack tip opening. The buckling behavior can be apparently seen from the misalignment of loading and unloading curves and from the photo taken at the end of the fracture experiment (refer to Figure C.2).

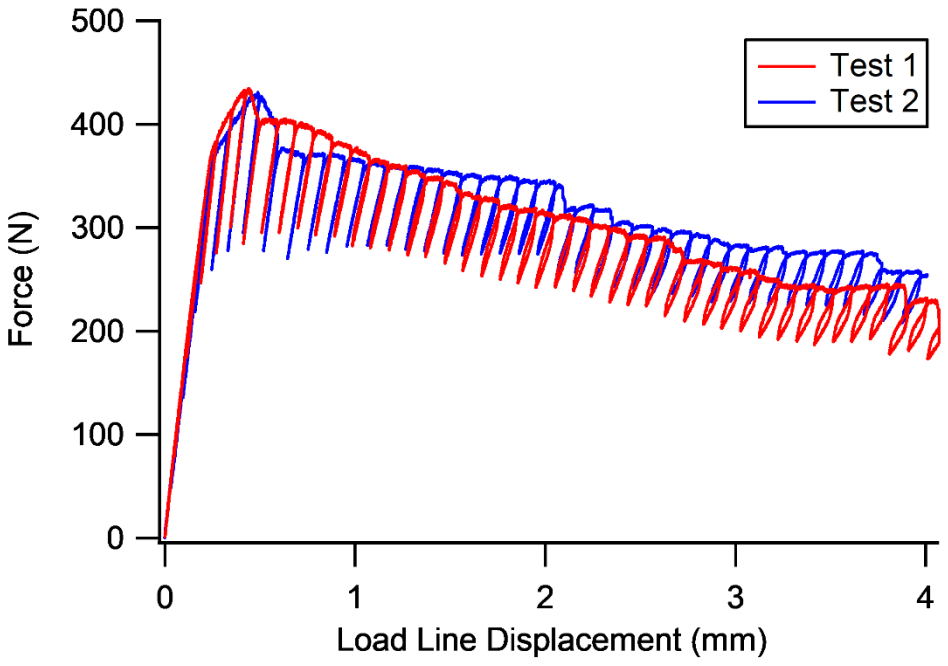

Figure C.1. Load-displacement curves for NiTi specimens having 1 mm thickness from Test 1 and Test 2

Figure C.2. Photo of the sample having 1 mm thickness buckled at the end of the fracture experiments

APPENDIX D

ELASTIC COMPLIANCE CORRECTION FOR SPECIMEN ROTATION

The rotation correction should be taken into account for geometry changes due to deformation for CT specimens. In accordance with ASTM E1820, the crack size estimation is corrected for rotation with the following compliance formula:

$$C_{c(i)} = \frac{C_i}{\left(\frac{H^*}{R_i}\sin\theta_i - \cos\theta_i\right)\left(\frac{D}{R_i}\sin\theta_i - \cos\theta_i\right)} \tag{D.1}$$

where C_i is the calculated elastic compliance at the i^{th} point, $C_{c(i)}$ is the corrected elastic compliance at the i^{th} point, H^* is the half distance between the center of the pin holes, $R_i = (W + a)/2$ is the radius of rotation at the i^{th} crack size, D is the half of the gauge length, θ is the angle of rotation having the following formula

$$\theta_i = \sin^{-1}\left(\frac{D + \frac{v_i}{2}}{\sqrt{D^2 + R_i^2}}\right) - \tan^{-1}\left(\frac{D}{R_i}\right) \tag{D.2}$$

where v_i is the total load line displacement at the beginning of the i^{th} loading/unloading cycle.